Journal Pre-proof

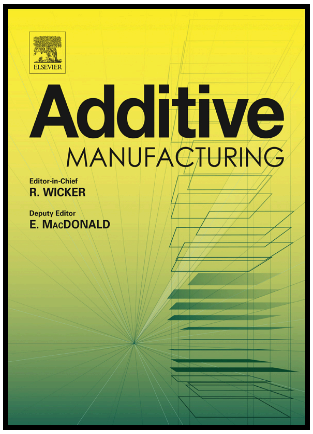

On the orientation-dependent mechanical properties of interstitial solute strengthened $Fe_{49.5}Mn_{30}Co_{10}Cr_{10}C_{0.5}$ high entropy alloy produced by directed energy deposition

Ali Chabok, Wei Zhang, Jiajia Shen, J.P. Oliveira, Hui Wang, Shaochuan Feng, Nobert Schell, Bart J. Kooi, Yutao Pei

PII: S2214-8604(23)00527-4
DOI: https://doi.org/10.1016/j.addma.2023.103914
Reference: ADDMA103914

To appear in: *Additive Manufacturing*

Received date: 29 August 2023
Revised date: 3 December 2023
Accepted date: 4 December 2023

Please cite this article as: Ali Chabok, Wei Zhang, Jiajia Shen, J.P. Oliveira, Hui Wang, Shaochuan Feng, Nobert Schell, Bart J. Kooi and Yutao Pei, On the orientation-dependent mechanical properties of interstitial solute strengthened $Fe_{49.5}Mn_{30}Co_{10}Cr_{10}C_{0.5}$ high entropy alloy produced by directed energy deposition, *Additive Manufacturing,* (2023) doi:https://doi.org/10.1016/j.addma.2023.103914

This is a PDF file of an article that has undergone enhancements after acceptance, such as the addition of a cover page and metadata, and formatting for readability, but it is not yet the definitive version of record. This version will undergo additional copyediting, typesetting and review before it is published in its final form, but we are providing this version to give early visibility of the article. Please note that, during the production process, errors may be discovered which could affect the content, and all legal disclaimers that apply to the journal pertain.

© 2023 Published by Elsevier.

On the orientation-dependent mechanical properties of interstitial solute strengthened $Fe_{49.5}Mn_{30}Co_{10}Cr_{10}C_{0.5}$ high entropy alloy produced by directed energy deposition

Ali Chabok[1#], Wei Zhang[1#], Jiajia Shen[3, 4], J.P. Oliveira[3,4], Hui Wang[2], Shaochuan Feng[5], Nobert Schell[6], Bart J. Kooi[2], Yutao Pei[1,*]

[1] Advanced Production Engineering, Engineering and Technology Institute Groningen, Faculty of Science and Engineering, University of Groningen, Nijenborgh 4, 9747 AG, the Netherlands

[2] Nanostructured Materials and Interfaces, Zernike Institute for Advanced Materials, Faculty of Science and Engineering, University of Groningen, Nijenborgh 4, 9747 AG, the Netherlands

[3] UNIDEMI, Department of Mechanical and Industrial Engineering, NOVA School Science and Technology, Universidade NOVA de Lisboa, Caparica 2829-516, Portugal

[4] CENIMAT/I3N, Department of Materials Science, NOVA School of Science and Technology, Universidade NOVA de Lisboa, 2829-516 Caparica, Portugal

[5] School of Mechanical Engineering, University of Science and Technology Beijing, Beijing 100083, China

[6] Institute of Materials Physics, Helmholtz-Zentrum Hereon, Max-Planck-Str. 1, Geesthacht, D-21502, Germany

Journal Pre-proof

Abstract

Interstitial solute-strengthened $Fe_{49.5}Mn_{30}Cr_{10}Co_{10}C_{0.5}$ (at%) high entropy alloy was additively manufactured by directed energy deposition (DED) process in this work. While the as-deposited material exhibits an excellent combination of strength and ductility, the effect of anisotropy on the mechanical performance of the DED processed component was studied in detail. The ultimate tensile strength (UTS) of the horizontal tensile sample with a main fiber texture of <111> // tensile direction (TD), went up to 1 GPa while maintaining a superb failure elongation of 36 %. The vertical tensile sample, with a dominant <001> // TD texture, failed at an UTS of 750 MPa with an enhanced failure elongation of 52%. Microstructural analysis of the deformed samples showed that the horizontal samples were mainly deformed via the formation of mechanical twins, whereas the twining activity was less profound in the vertical samples. Single crystal micro-pillar compression testing revealed that the deformation

---

[#] Equally contributed

[*] Corresponding author. Email address: y.pei@rug.nl

mechanism complies well with the Schmid's factor. In addition, a higher critical resolved shear stress for twining compared to slip was also confirmed in the micro-pillar compression testing.

Graphical abstract

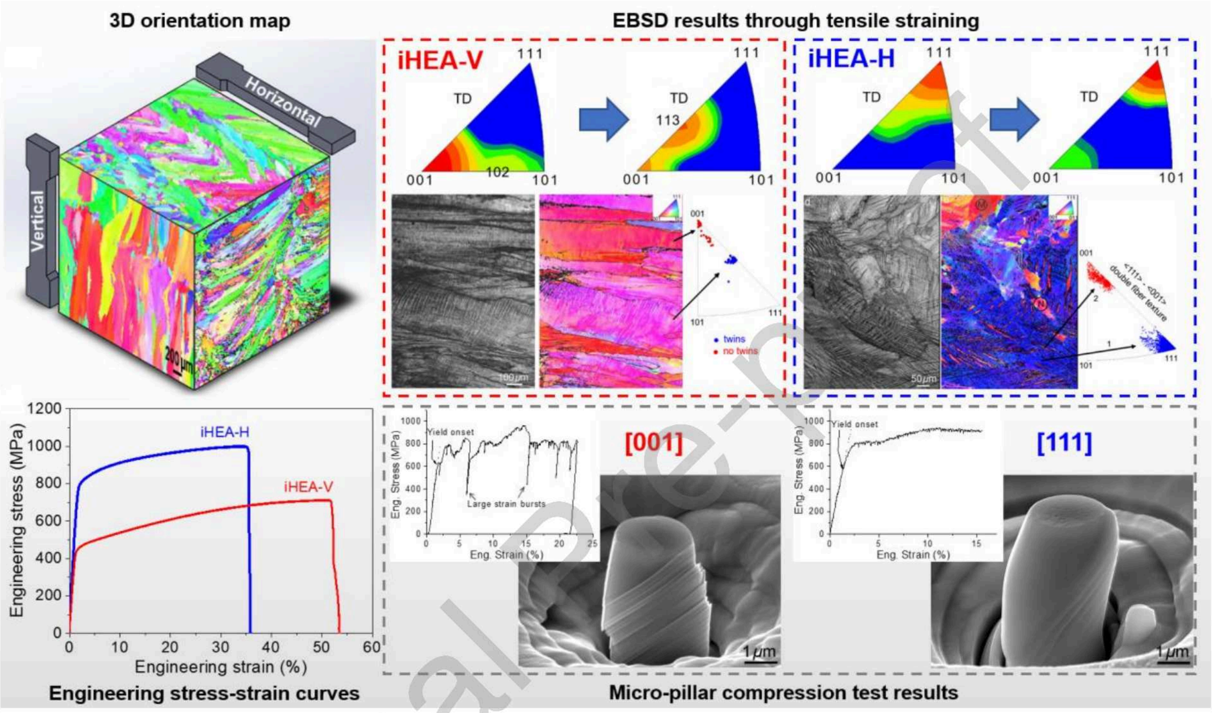

Keywords: Directed energy deposition, high entropy alloy, interstitial solute strengthening, precipitation strengthening, deformation mechanism, mechanical properties

1. Introduction

In recent years, high entropy alloys (HEAs), as multi-principal element alloying systems, have attracted significant attention owing to their superior combination of strength and ductility [1-3]. The original idea of HEA was developed based on the equiatomic ratio of multiple principle elements to obtain a stabilized single-phase solid solution due to the maximization configurational entropy of the alloying system [4]. However, recent studies have shown that the formation of single-phase solid solution is less dependent on the maximized configurational entropy [5,6]. Yao et al. [7] developed a non-equiatomic FeMnNiCoCr HEA and showed that massive solid solution can form over a broad composition range. Non-equiatomic HEAs paved the way for exploring new HEA compositional spaces by adding interstitial elements. Oxygen-doped TiZrHfNb HEA

Journal Pre-proof

exhibited enhanced strength and ductility through the formation of oxygen complexes [8]. Wu et al. [9] added carbon to the composition of fcc single-phase HEA and reported higher strength and ductility due to the formation of nanotwins. In another work [10], the doping of 30 ppm boron into non-equiatomic $Fe_{40}Mn_{40}Cr_{10}Co_{10}$ (at%) HEA resulted in simultaneously enhanced yield strength, ultimate tensile strength (UTS) and ductility.

The interstitial carbon-added dual-phase non-equiatomic $Fe_{49.5}Mn_{30}Cr_{10}Co_{10}C_{0.5}$ (at%) is a relatively new class of HEAs with excellent synergy of strength and ductility [11]. It has been reported that the addition of carbon leads to simultaneous activation of twining and phase transformation induced plasticity (TWIP and TRIP) during uniaxial tensile testing [11]. The TWIP and TRIP deformation mechanisms together with other strengthening mechanisms such as interstitial solid solution strengthening and precipitation strengthening culminate in significant increase in strength and ductility compared to the single-phase HEA with the same composition [12].

While most studies have focused on HEAs produced by casting and post-processing steps such as hot and cold rolling, forging and solution annealing to tailor the microstructure and mechanical properties, the laser additive manufacturing (LAM) methods have been emerging as versatile fabrication routes for HEAs, offering near-net-shape production of complex geometries [13-16]. Directed energy deposition (DED) is one of the LAM techniques suitable for producing large-scale complex metal components. With DED, a powerful laser beam produces a molten pool on a self-supporting substrate that is built up in a layer-wise manner. The metal powder is injected coaxially with the laser beam into the molten pool (blown powder), where the powder is melted and metallurgically bonded to the previous layer. This enables new layers of metal materials with desired properties to be applied to create 3D structures. Haase et al. [17] used an elemental powder blend to fabricate equiatomic CoCrFeMnNi HEA by DED. Significantly reduced segregation and pronounced texture have been observed for the DEDed HEAs compared to the as-cast counterparts. Higher yield strength and UTS was also reported in DEDed CoCrFeMnNi HEA [18] due to its finer microstructure.

There are limited number of reports on the LAM of interstitial-strengthened $Fe_{49.5}Mn_{30}Cr_{10}Co_{10}C_{0.5}$ (at%) HEA (iHEA). Laser powder bed fusion (LPBF) of the iHEA was reported in [19]. The results showed that the additively manufactured iHEA achieves higher strength but lower ductility compared to the cast product. Additionally, while the cast iHEA showed fcc and hcp dual-phase structure, fcc single-phase structure was observed in the as-printed iHEA. DED process was also applied to produce this iHEA by Chew et al. [20].

Journal Pre-proof

They reported similar mechanical properties to that of LPBFed iHEA. While TWIP and TRIP activation were observed for the room-temperature tensile test of the DEDed iHEA, low-temperature tensile testing at -40 °C and -130 °C showed only the TRIP effect. A fine cellular structure together with oxide inclusions was reported as the main strengthening mechanisms for the printed iHEA.

To the best of our knowledge, there are no reports on the effect of anisotropy resulting from the DED process on the microstructure and mechanical properties of $Fe_{49.5}Mn_{30}Cr_{10}Co_{10}C_{0.5}$ iHEA. The current study aims to explore the effect of texture on the mechanical properties and deformation mechanism of DEDed iHEA. Tensile testing and micro-pillar compression tests are utilized to evaluate the orientation-dependent mechanical performance of the additively manufactured iHEA.

2. Experimental

DED process was carried out using a 3 kW IPF Photonics fiber laser with a wavelength of 1.07 μm. Gas atomized pre-alloyed powder with a nominal composition of $Fe_{49.5}Mn_{30}Cr_{10}Co_{10}C_{0.5}$ (at.%) and size distribution of 50-140 μm was delivered to the melt pool on ST37 plain carbon steel substrate. The particle morphology and EDS elemental mapping of the iHEA powders are shown in Fig.1. All elements are uniformly distributed in the pre-alloyed powders, and the detailed chemical composition of the powders is listed in Table 1. The trace presence of O is considered to be related to the contamination during powder fabrication process. The iHEA components were additively manufactured using a laser power of 1500 W, laser beam spot of 3 mm in diameter, laser beam scanning speed of 350 mm/min and an overlap ratio of 50%. The deposition process was carried out with Ar gas shielding. Bidirectional scanning strategy was utilized through which the laser scanning direction changes for each deposition layer (Fig. 2a). Fig. 2b shows a typical deposited block of iHEA with 40 mm length, 15 mm thickness and 17 mm height. The measured chemical composition of the as-deposited samples is listed in Table 1, where the contents of metallic elements were measured by EDS, while the contents of C and O were measured by inductively coupled plasma-atomic emission spectroscopy.

Table 1 Chemical composition of the iHEA powders and as-deposited samples (at.%).

Element	Fe	Mn	Co	Cr	C	O
iHEA powder	45.88	33.80	8.58	11.16	0.50	0.08
DED iHEA sample	47.82	30.80	9.15	11.51	0.53	0.19

Journal Pre-proof

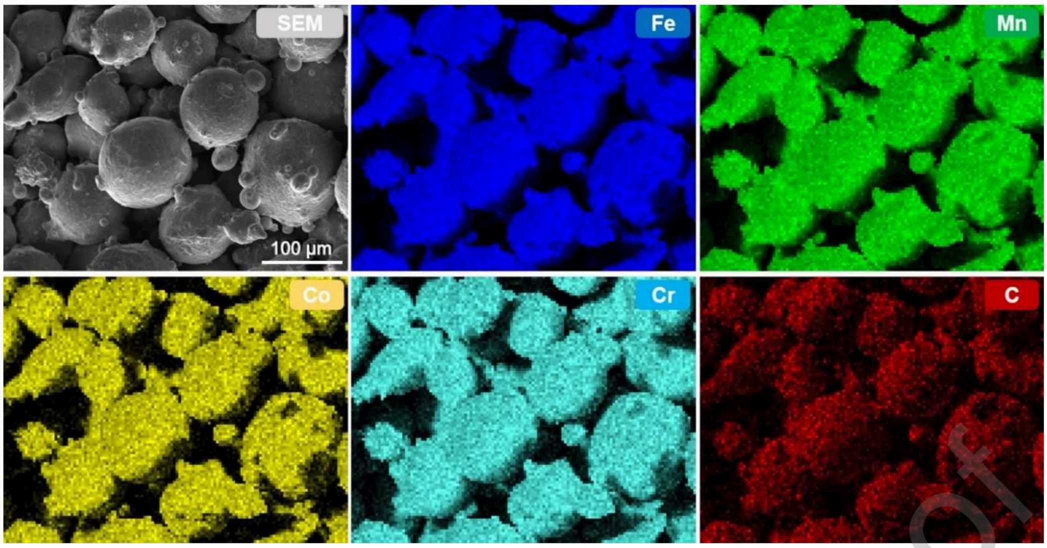

Fig. 1 Particle morphology as revealed by SEM and SEM-EDS elemental mapping results of pre-alloy $Fe_{49.5}Mn_{30}Cr_{10}Co_{10}C_{0.5}$ iHEA powders.

The microstructure of the deposited samples was examined by scanning electron microscopy (SEM) and electron back scatter diffraction (EBSD) on a Tescan Lyra dual beam SEM-FIB microscope. To investigate the mechanical performance of the deposited iHEA material, tensile specimens with the gauge dimension of 11.5 mm × 3.5 mm × 1 mm were machined from the deposited block in two different directions, as schematically shown in Fig. 2c. The 3D inverse pole figure (IPF) map represents a typical microstructure of the grains in the DED deposited iHEA. Vertical sample labeled as iHEA-V was machined parallel to the building direction (BD) and the horizontal tensile sample named as iHEA-H was sliced parallel to the laser scanning direction. The tensile test was carried out using a Kammrath-Weiss tensile module with a strain rate of 10^{-4} s^{-1}, and the machine displacement was used to measure strain. High-energy synchrotron X-ray diffraction (SXRD) was applied to analyze the phase constituents before and after tensile deformation. To further determine the deformation mechanisms, transmission electron microscopy (TEM) analysis was performed on grains with different orientations. The TEM samples were prepared using focused ion beam (FIB) slicing (Tescan Lyra dual beam microscope). Micro-pillar compression test was used to evaluate the micro-mechanical properties of deposited iHEA in two different crystal orientations close to [001] and [111], respectively. Micro-pillars with a diameter of 2 μm and length of 6-7 μm were fabricated using FIB with 10 and 3 nA ion currents during the initial rough milling process. 200 and 40 pA ion currents were used for the final polishing steps. An ion-milled micro-pillar and schematic of the micro-pillar compression test by a flat diamond punch are shown in Fig. 3a and 3b, respectively. The white circles in the IPF maps presented

Journal Pre-proof

in Fig. 3c and 3d illustrate the selected areas for the micro-pillar milling through [001] and [111] directions, respectively.

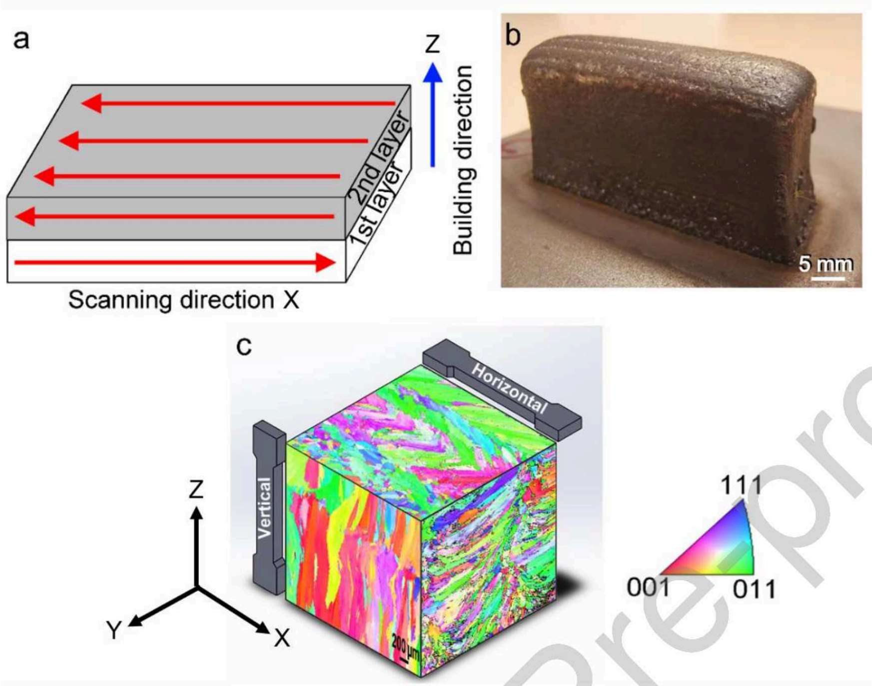

Fig. 2 (a) Laser scanning strategy, (b) as-deposited iHEA block and (c) 3D inverse pole figure (IPF) representing the overall microstructure.

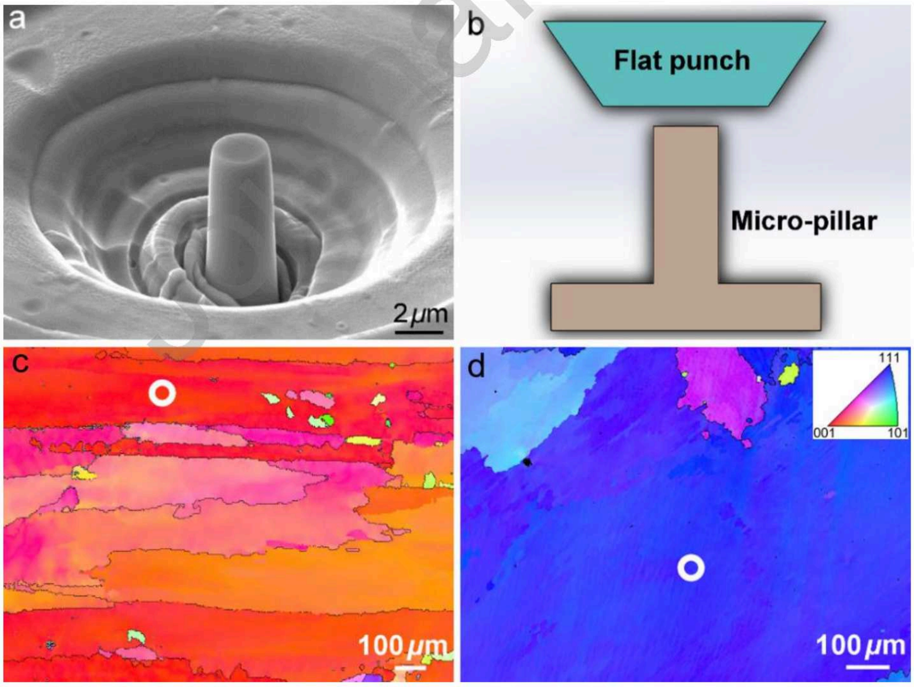

Fig. 3 (a) SEM image of ion-milled micro-pillar, (b) schematic image of the micro-pillar compression by a flat punch. IPF maps with a white circle indicating the selected area for milling a micro-pillar oriented along (c) [001] and (d) [111] orientations. The IPFs were plotted relative to the normal direction of samples.

Journal Pre-proof

3. Results and discussion

3.1 As-deposited microstructure

An optical microscopy image of the as-built iHEA in the cross-section normal to the laser scanning direction is shown in Fig. 4a. A layer-by-layer deposition pattern with an average thickness of 650 μm and ripple-like melt pool with an average size of 573 ± 180 μm can be seen. A mixed columnar and equiaxed grain structure solidified inside the melt pool, as shown in Fig. 4b. Higher magnification SEM images of the equiaxed and columnar grains are shown in Fig 4c, and 4d, respectively. The secondary arm spacing of the dendritic structure is very small and a cellular solidification substructure can be observed in Fig. 4c. The IPF of the marked square area in Fig. 4a, along the BD together with the indicated melt pool boundaries, is presented in Fig. 4e. It illustrates the epitaxial grain growth extending over several layers, with the major grain orientation of <001> and <011> // BD. It should be noted that the melt pool boundary lines are added here to help understand the relative positional relationship between the grain morphology and the laser melt pool, which were not directly identified from the IPF map due to the epitaxial growth of many grains. The phase map with the superimposed grain boundary map is depicted in Fig. 4f, showing that the as-deposited structure is almost entirely composed of fcc phase, with columnar grains mainly separated by high-angle grain boundaries (HAGBs).

Journal Pre-proof

Additionally, it is worth noting that the IPF in Fig. 2c reveals different grain morphologies between the two side planes (i.e., X-Z and Y-Z planes). In the sample preparation process of current work, the laser scanning direction is along the X direction, and a 180° turn is applied to two consecutive deposition layers (Fig. 2a), which means that the thermal gradients along the X and Y directions during the laser deposition process are different, resulting in different microstructures in these two side planes. Specifically, on the X-Z plane, the melt pool with a large width-to-height ratio of the current LMD process enlarges the remelting regions, thereby favoring the alignment of the maximum thermal gradient direction along the BD (Z direction), promoting the epitaxial growth of pre-existing grains and the resulting formation of elongated columnar grains across multiple deposition layers [21]. Consequently, a strong <001> orientation along the BD was formed, where the <001> is the preferable growth direction for cubic crystals [22]. Besides, competitive growth occurs under the influence of local heat flux perturbations related to the movement of the laser beam along the X direction in the dynamic melt pool [21], resulting in a weak <101> texture along the BD in the as-deposited sample. In comparison, on the Y-Z plane as shown in Fig. 4a, the temperature gradient direction perpendicular to the local melt pool boundary in a semielliptical shaped melt pool, promotes the growth of <001> grains from the local melt pool boundary towards the center of the melt pool. As such, epitaxial growth with <101> orientation along the BD is formed. Meanwhile, current bidirectional laser scanning strategy leads to local perturbations in heat flux, causing the solidified grains to shift their growth direction towards new directions along local temperature gradients [23]. These new growth directions may no longer be preferable for continuous growth, thus leading to competitive growth of cellular dendrites even inside a melt pool on the Y-Z plane [22], this can also be confirmed by the fine dendritic structure in Fig. 4b and 4d. Hence, the development of different microstructures on X-Z and Y-Z planes results from the competition between the alignment of preferable growth directions and the directions of local thermal gradients [21, 24].

Pre-proof

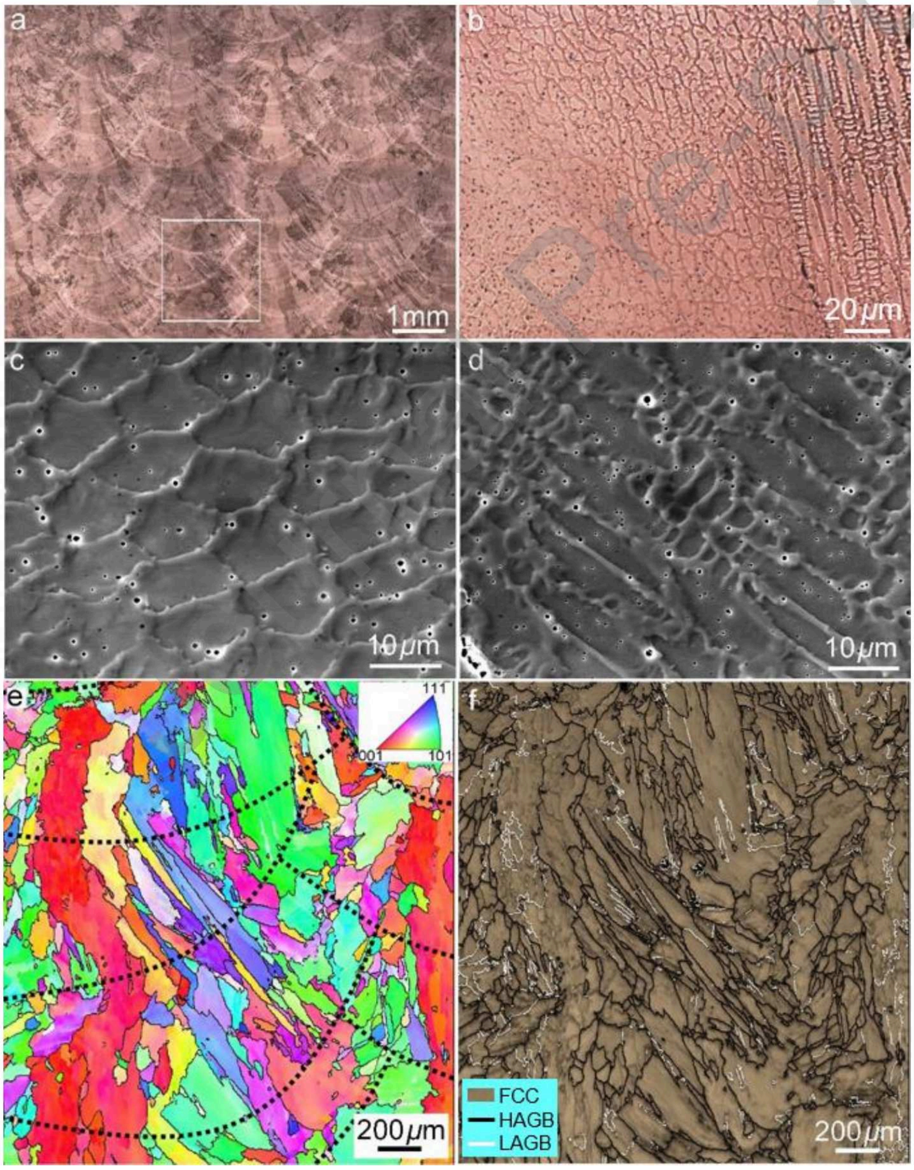

Fig. 4 (a) Optical macrograph from the cross-section normal to the laser scanning direction and (b) fine dendritic structure in the melt pool. SEM image of the (c) equiaxed and (d) columnar dendritic structure. (e) IPF map of the marked square area in (a) with melt pool boundaries indicated as dashed black lines, (f) the corresponding phase map with superimposed grain boundaries map.

To precisely determine the existing phases and the corresponding phase fractions, high-energy SXRD was applied for the as-deposited sample. The obtained diffraction pattern is presented in Fig. 5. In addition to the fcc phase observed by EBSD, $M_{23}C_6$ and M_7C_3-type precipitates were also detected, which is attributed to the excellent signal-to-noise ratio of synchrotron X-ray sources enabling phase identification and quantification of even minority phases. According to the Rietveld refinement, the phase fractions of fcc, $M_{23}C_6$ and M_7C_3 are calculated as 98.29%, 1.06% and 0.65%, respectively.

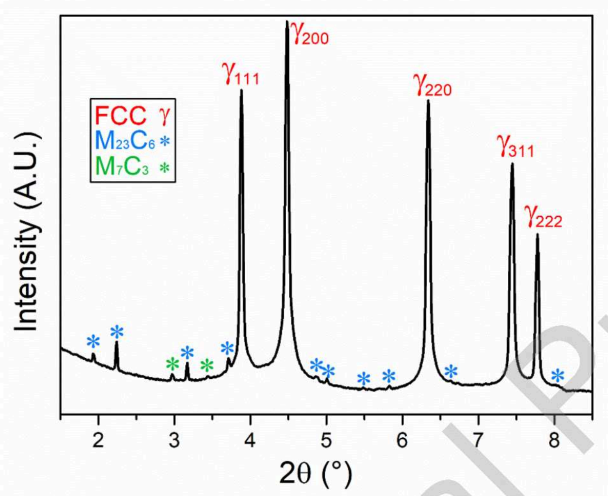

Fig. 5. High-energy SXRD pattern of as-deposited iHEA sample.

Fig. 6a shows the SEM-EDS elemental distribution of the equiaxed grain structure. While Co and Cr are uniformly distributed inside and at the boundaries of the subgrains, there is, despite the rapid cooling of the DED process, Mn segregation towards the cellular boundaries and Fe segregation towards the interiors. These results are in good agreement with [25-27], where the HEAs with high Mn content show Fe and Mn segregation to the cell interiors and boundaries, respectively. Laurent-Brocq et al. [27] studied the thermodynamics of the CoCrFeMnNi HEA using an analogy with fully miscible binary alloys and reported that the solidus and liquidus temperatures of $Mn_{50}Ni_{50}$ are lower than those of $Fe_{33}Co_{33}Cr_{33}$. Therefore, as the temperature in the molten pool drops to the liquidus point, the dendrites start to solidify preferentially enriched in Fe, Co and Cr and subsequently the Mn- and Ni-rich phases solidify in the interdendritic spacing. Kies et al. [28] reported the interdentritic segregation of Mn and C in DEDed high Mn steel despite the high cooling rate of the solidification process. Slight segregation of C element is also observed at the subgrain boundaries in Fig. 6a, indicating the possibility of carbide formation. In order to observe the carbides more clearly, we acquired backscattered electrons (BSE) signals on the surface of the sample etched with Waterless Kalling's etchant. The obtained BSE image is shown in Fig. 6b, where Fig. 6b1 and 6b2 are corresponding BSE and SE images of the magnified area marked with a red box in Fig. 6b. Significant aggregation of nano-scale carbides can be observed at the cellular boundaries. In addition to elemental segregation, uniformly distributed near-spherical particles are also observed in the as-built iHEA. The TEM and high resolution TEM (HRTEM) images, SAED pattern and the TEM-EDS results in Fig. 6b-e confirm the fcc-structured Mn-rich oxide and sulfide precipitates in the iHEA matrix. The local enrichment of O and S is related to the contamination during the powder fabrication process [29], and the former is also considered to be closely related to the current DED process where the Ar gas shielding was not sufficient enough to fully protect the melt pool from oxygen.

Journal Pre-proof

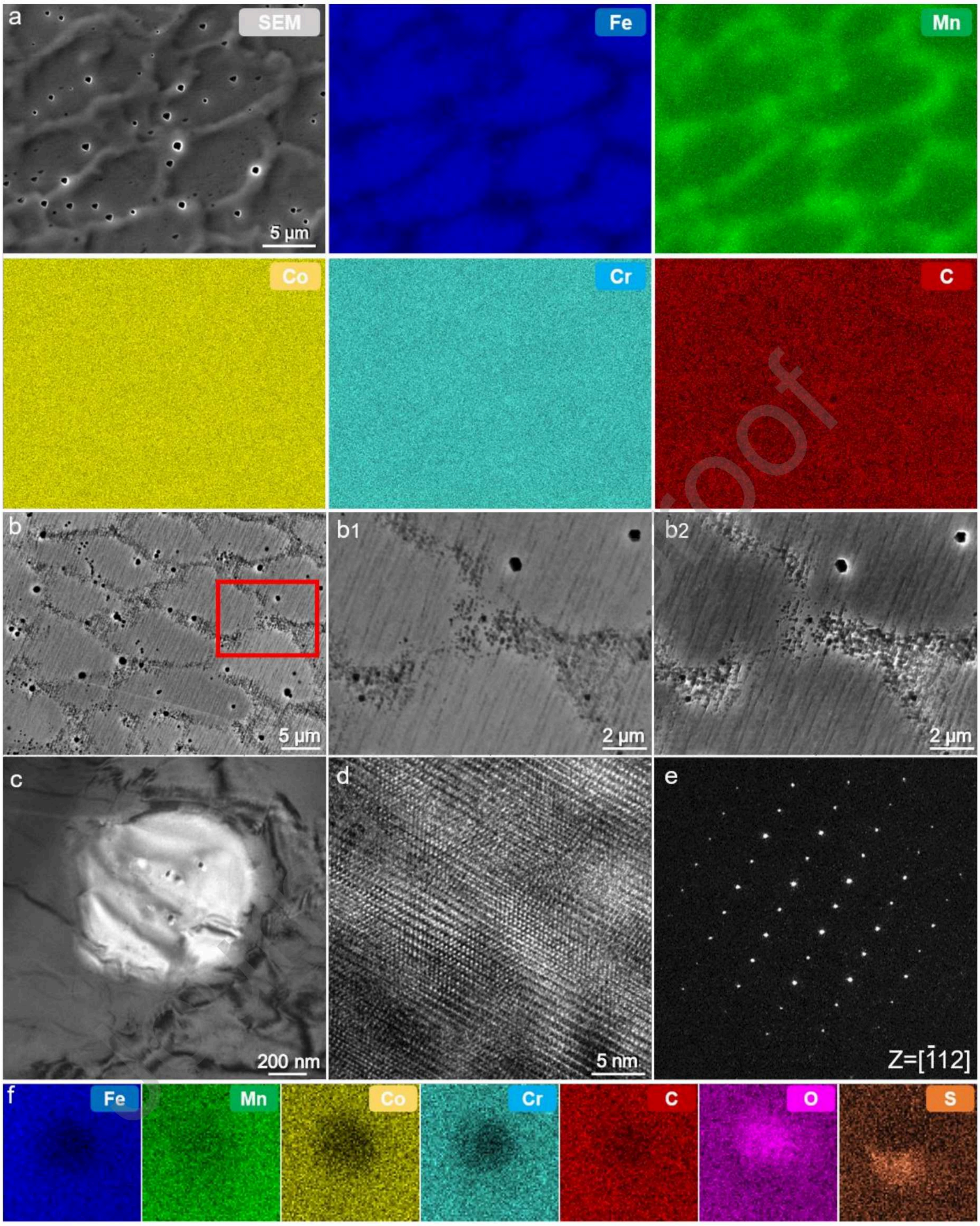

Fig. 6 (a) SEM-EDS element mapping of equiaxed cellular structure. (b) BSE image showing the carbides at cellular boundaries, (b1) and (b2) are corresponding BSE and SE images of the magnified area in (b). (c) TEM and (d) HRTEM micrographs of the precipitate, (e) the corresponding SAED pattern, (f) TEM-EDS mapping of the precipitate in (c).

3.2 Orientation-dependent mechanical properties

3.2.1 Tensile testing

The representative engineering stress-strain curves for the DEDed iHEA components are shown in Fig. 7a. The yield strength (σ_y) of the iHEA-V sample is about 430 MPa and its ultimate tensile strength (σ_{UTS}) goes up to 750 MPa with the failure elongation of 52%. The iHEA-H sample shows significant increase in the σ_y and σ_{UTS} to about 790 MPa and 1000 MPa, respectively, while enduring a slightly reduced elongation of 36 %. The trade-off between ductility and strength of these samples are evident.

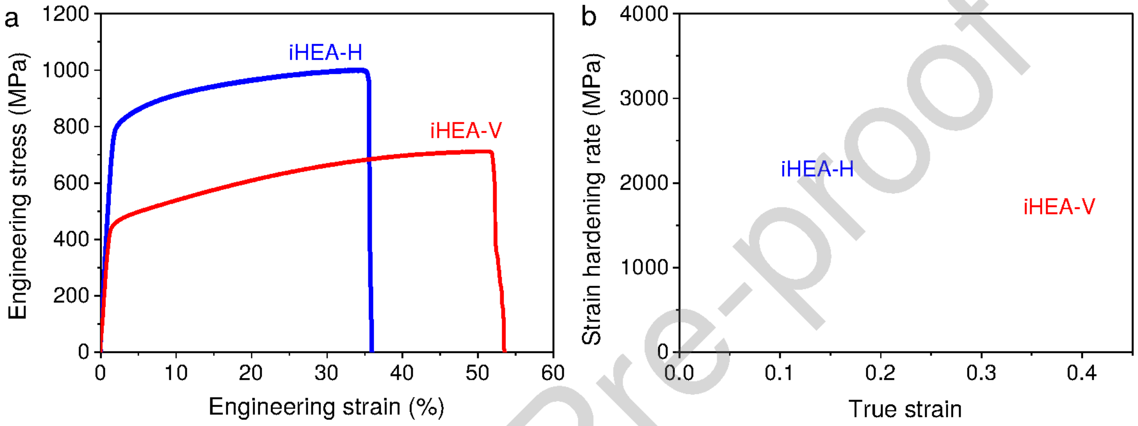

Fig. 7 (a) Engineering stress-strain curves and (b) corresponding strain hardening rate curves of the DEDed iHEA tensile samples taken, with respect to building, along horizontal (H) and vertical (V) directions.

The corresponding strain hardening rate (SHR) curves for these two samples are presented in Fig. 7b. The iHEA-H reveals slightly higher SHR compared to the iHEA-V sample, especially at lower strains. Followed by a fast decrease in SHR after yielding up to 0.05 true strain, the iHEA-H sample shows a slower reduction in SHR until 0.1 true strain. The SHR then changes insignificantly until sample rupture. The iHEA-V sample shows comparable SHR compared with the iHEA-H sample despite its lower tensile strength. After a sharp decline in SHR till 0.03 true strain, there is a steady and small increase in SHR up to 0.2 true strain followed by slow and steady reduction until failure point. Fig. 8 compares the tensile properties of different classes of as-deposited HEAs produced using DED. The graph shows an excellent strength-ductility synergy of the iHEAs presented in this work, pushing the paradigm for the tensile properties of additively manufactured HEAs.

Journal Pre-proof

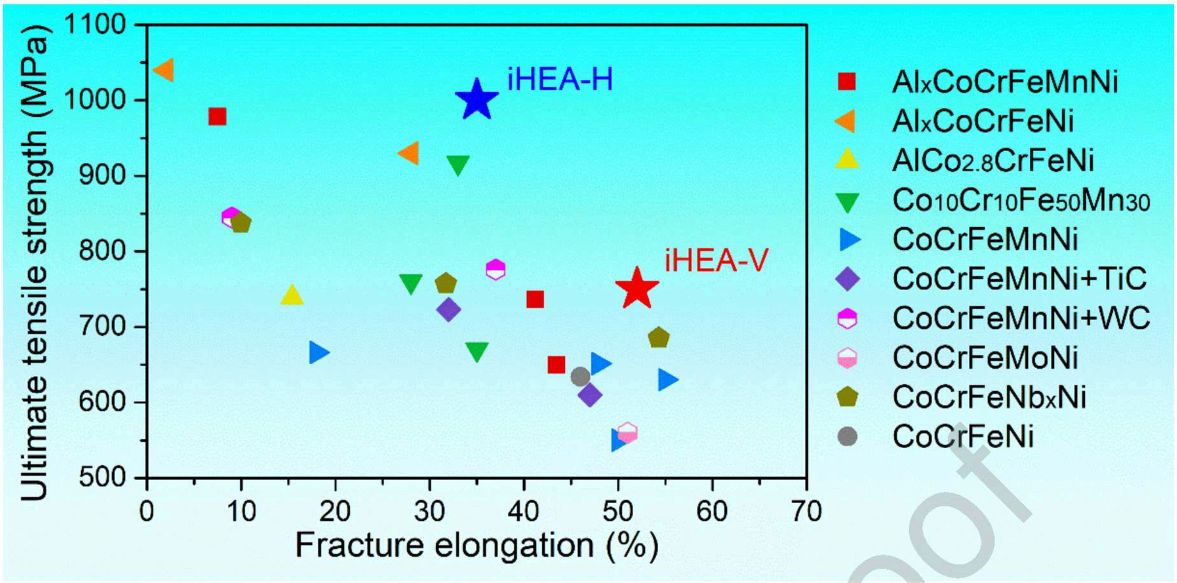

Fig. 8 Comparison of UTS and elongation of HEAs produced by laser melting deposition according to literature [30-40] with those obtained in the present work (iHEA-H and -V).

3.2.2 Texture and deformation mechanisms analysis

Fig. 9 depicts the orientation distribution function (ODF) at the φ_2=45 section and IPF texture of the tensile samples before deformation. The IPFs indicate how the grains are oriented in relation to the tensile direction (TD) as a reference axis. The main texture components of the samples described in {hkl}<uvw> parallel to the tensile plane and main fiber parallel to the TD are presented in Table 2. The as-deposited iHEA shows strong anisotropy in texture in horizontal and vertical directions. The main texture components of the iHEA-H sample before deformation are Copper and A with the main fiber texture of <111> // TD (Fig. 9a, c). Fig. 9b shows the ODF of the iHEA-V sample with a totally different texture composed of Goss, Cube and rotated Copper components. As shown in Fig. 9d, the main texture fiber for the iHEA-V sample is <001> // TD. There is also a minor texture around <102> // TD, deviating slightly from <101> // TD. The evolved texture in the iHEA-V sample is ascribed to the preferred primary dendrites growth of <001> direction towards the maximum heat flux in cubic materials, which is almost parallel to the BD. The presence of the minor fiber texture close to <102> // TD may arise from the fact that the dendrites tend to grow normal to the melt pool boundaries. Since these boundaries are curved, the grains nucleated at the sides of the melt pool grow in a direction tilted with respect to the BD of the sample.

The φ_2=45 ODF sections and IPFs of the tensile samples after fracture are shown in Fig. 10. The iHEA-H sample after fracture still shows the main A texture component with the fiber texture <111>// TD. However, the Copper texture component in the iHEA-H sample before deformation disappears and instead a minor Goss texture emerges during deformation (Fig. 10a). The IPF of the deformed iHEA-H sample in Fig. 10c confirms that the main fiber texture of <111> // TD is retained after fracture, and it is now combined with a minor fiber texture of <001> // TD related to the Goss texture. The texture evolution for the iHEA-V sample after fracture is shown in Fig. 10b and d. As seen, there is no longer rotated Copper texture in the case of the deformed iHEA-V sample. A minor Cube texture is still present but the main texture is around <113>, slightly deviating from the Goss component. The IPF in Fig. 10d clearly demonstrates two main fiber textures of <001> and <113> parallel to the TD in the deformed vertical sample.

Table 2 Main texture components in {hkl}<uvw> notations and the corresponding fiber texture.

Symbol	Texture component	{hkl}<uwv>	Fiber
▲	A	{110}<1-11>	<111> // TD
C	Copper	{112}<-1-11>	<111> // TD
RC	Rotated Copper	{112}<1-10>	<101> // TD
■	Cube	{001}<100>	<001> // TD
◆	Goss	{110}<001>	<001> // TD

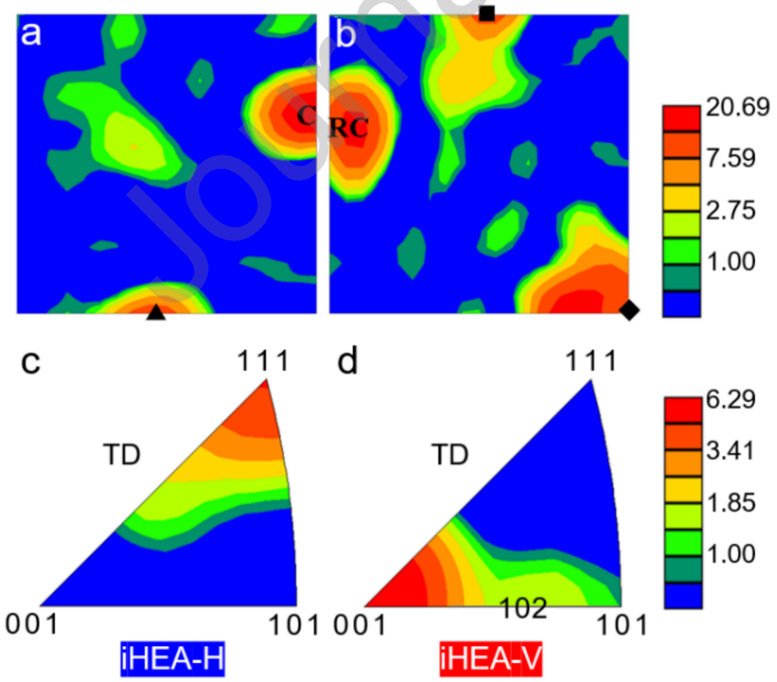

Fig. 9 φ_2=45 ODF sections and IPF texture of (a, c) iHEA-H and (b, d) iHEA-V tensile samples with respect to the reference axis of TD before deformation.

Journal Pre-proof

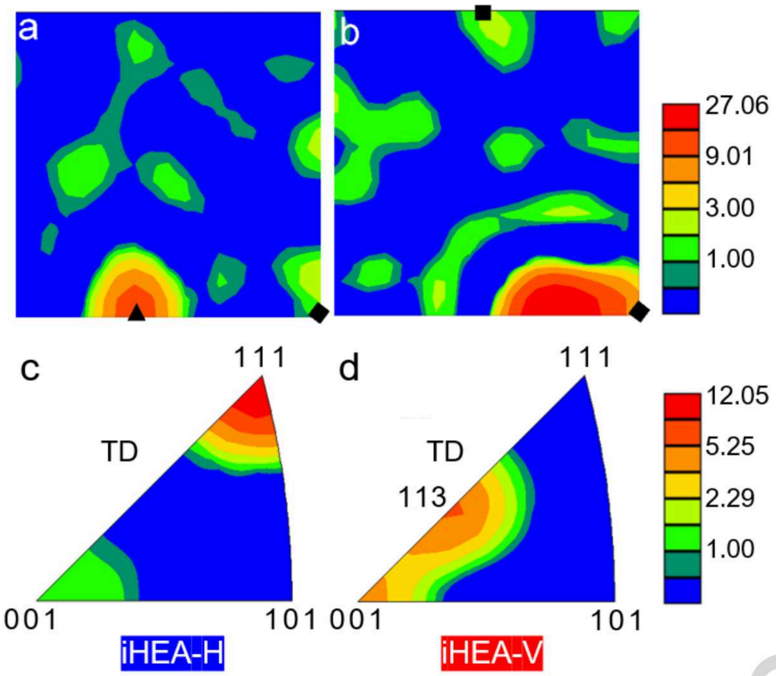

Fig. 10 φ_2=45 ODF sections and IPF texture of (a, c) iHEA-H and (b, d) iHEA-V tensile samples with respect to the reference axis of TD after tensile deformation.

The IPF maps of the tensile samples plotted relative to the TD are shown in Fig. 11. The zigzag structure of the grains in the iHEA-H sample clearly indicates the traces of the laser scanning track (Fig. 11a). A dominant <111> // TD texture, indicated by the blue grains, can be observed. In the case of the iHEA-V sample, the red large columnar grains have their <001> axis parallel to the BD (Fig. 11c). Furthermore, there are some grains oriented at 45º angle with respect to the BD, mostly with <101> and <102> axes along the BD.

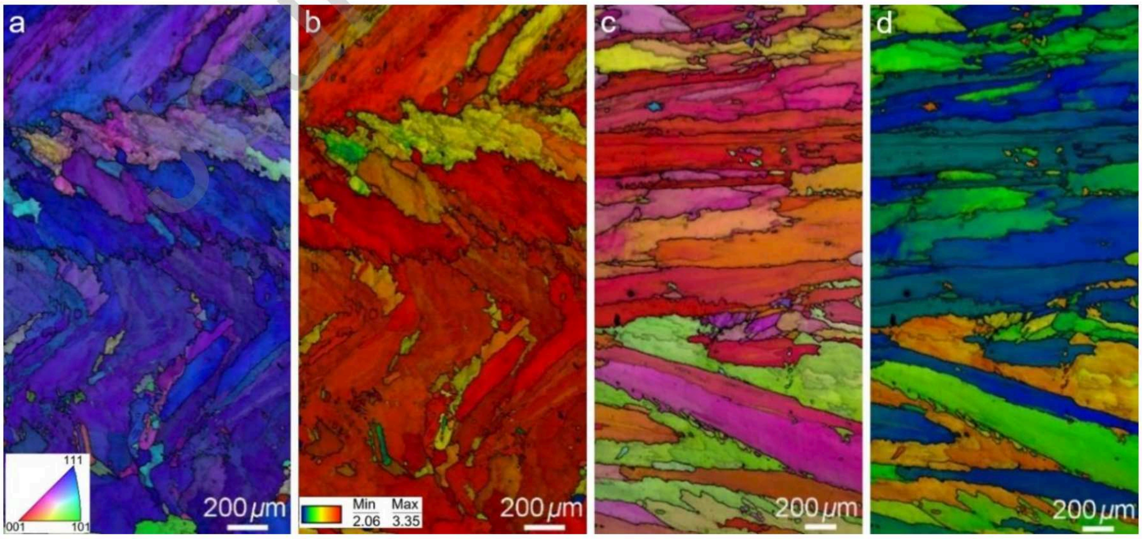

Fig. 11 IPF maps of (a) iHEA-H and (c) iHEA-V tensile samples plotted relative to the TD direction; (b, d) the corresponding Taylor factor map of iHEA-H and iHEA-V tensile samples, respectively.

Journal Pre-proof

Fig. 12 represents the microstructural changes in iHEA-H sample through straining during tensile test. No significant changes are detected by EBSD up to a true strain of 0.07 (Fig. 12a). As shown in Fig 12b, at a true strain of 0.14, some primary twin boundaries (TBs) in red can be detected by EBSD. However, it was already shown by Barbier et al. [41] that the twinning activity starts at earlier deformation steps and it can explain a slower reduction in SHR at lower deformation strains up to 0.1 (Fig. 7b). The IPF map in Fig. 12c at the true strain of 0.28 indicates the formation of more and thicker twins. It can also be observed that the grains with <111> // TD fiber texture are favorable for deformation twining. Moreover, some secondary twins with different configuration are detected inside the blue grain with <111> // TD fiber texture. The image quality (IQ) and IPF maps of the deformed iHEA-H sample after tensile test are given in Fig. 12d and 12e, respectively. The TBs are highlighted in black in Fig. 12e. The IQ and IPF images after fracture clearly indicate the formation of a large density of mechanical twins in the iHEA-H sample. As shown, the twin bundles are normally thicker than 100 nm and can be easily indexed by EBSD. Fig. 12e also confirms the formation of secondary activated twins with different configuration inside the grains with <111> // TD fiber texture.

Journal Pre-proof

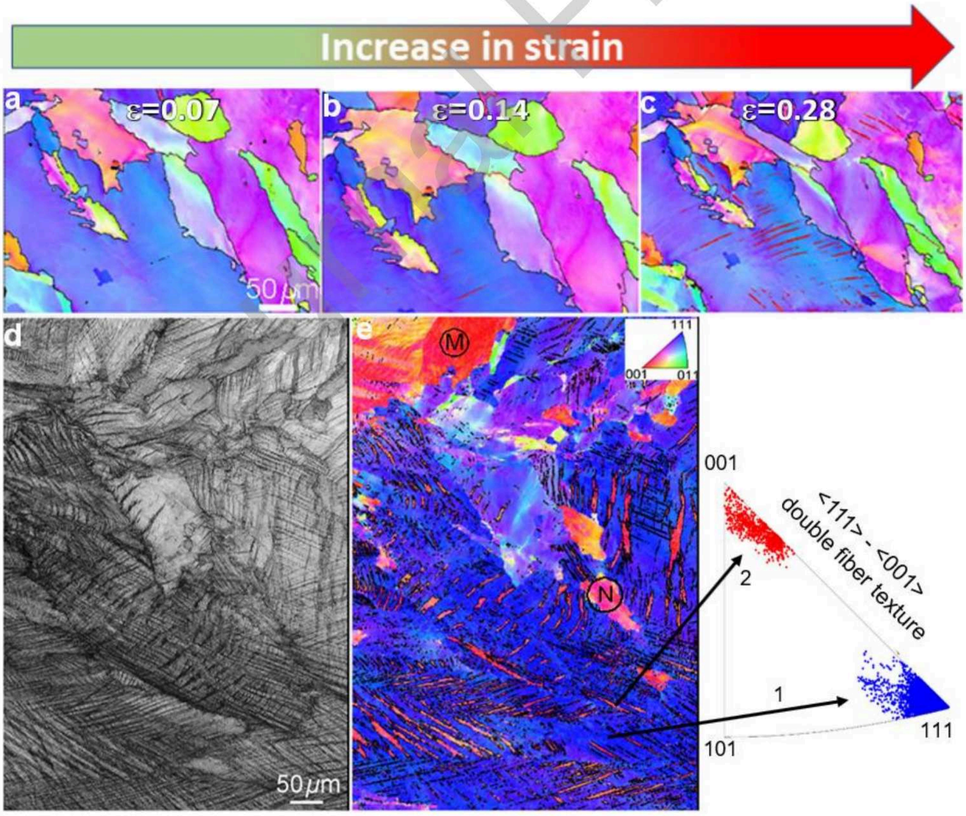

Fig. 12 (a-c) IPF maps showing the microstructural change in iHEA-H sample through tensile straining. (d) IQ and (e) IPF map of the failed iHEA-H sample together with the orientation of twined area inside the blue grains with <111> // TD fiber texture.

The misorientation angle distribution for the horizontal sample before and after deformation is shown in Fig. 13a. The fractured sample shows a sharp peak around 60º corresponding to the Σ3 twin boundary (60º around <111>). The results obtained elucidate the TWIP deformation mechanism of the horizontal samples. The grain orientation dependency of twin formation for the iHEA-H sample is shown in Fig. 13b. The blue dots indicate the orientation of some grains twinned during tensile deformation and the red dots are the orientation of the grains without twining after deformation. The results reveal that mechanical twining occurs mainly inside the grains with primary orientation of <111> // TD. On the other hand, limited or no twining is observed in the case of the grains orientated towards <001> // TD. This can also be observed from Fig. 12e, where the red grains labeled as M and N with <001> // TD orientation contain no twins even after fracture. Fig. 12e also explains the textural evolution of the horizontal sample after fracture in Fig. 10a and c. The arrow #1 indicates the orientation of the blue grains with <111> // TD fiber texture that are twinned during tensile deformation. The arrow #2 corresponds to the twinned area inside the blue grains, which enhances the <001> // TD fiber texture after fracture. In fact, deformation induced twinning inside the major fiber texture of <111> // TD leads to the minor texture of <001> // TD as already presented in Fig. 10a and 10c. It is consistent with the previous study in which the uniaxial tensile deformation of fcc materials led to the formation of <111> and <001> double fiber texture [42]. It was shown that <111> orientated grains remain stable during uniaxial tensile deformation, and in the case of the materials with low stacking fault energy, the emergence of <001> fiber texture is ascribed to the volume effect of twins through which the <111> grains are orientated by twins towards an <115> intermediate orientation. The final <001> orientation is subsequently formed by the rotation of <115> orientation through slip [42].

Journal Pre-proof

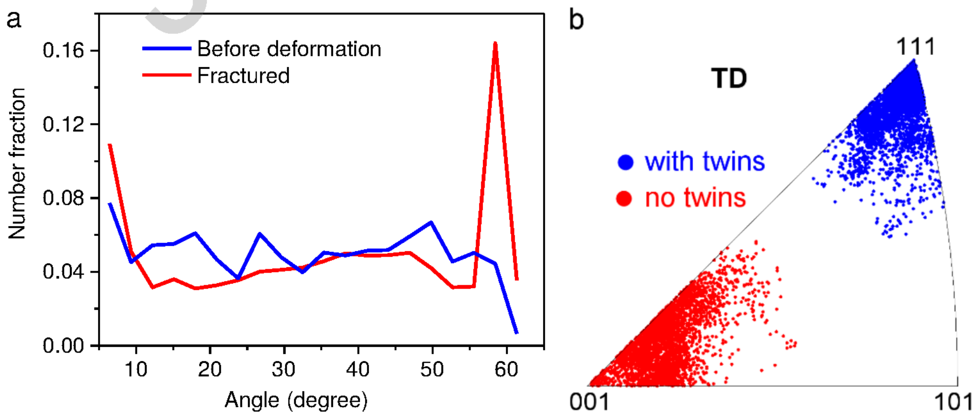

Fig. 13 (a) Misorientation angle distribution of iHEA-H tensile sample before and after tensile deformation, (b) IPF along the TD showing the orientation of grains containing mechanical twins in blue and grains without twins in red.

Fig. 14 depicts how the orientation of the microstructure evolved for the iHEA-V sample during uniaxial tensile test. The sample is characterized by the major <001> // TD and minor <101> // TD fiber textures before deformation (Fig. 9d). Two grains labeled as X and Y in Fig. 14a represent the <100> // TD and <101> // TD orientations, respectively. Through straining, the orientation of grain X remains almost unchanged (red grain with <100> // TD), whereas grain Y experiences a significant grain rotation during tensile test. Fig. 14e reveals the change in the average orientation of grain Y from its initial state until true strain of 0.38. As illustrated, the initial orientation of <101> rotates gradually towards the straight line connecting <001> and <111>, but closer to <111> orientation. Fig. 14 displays the misorientation profile along the black arrow indicated in Fig. 14d. Prominent peaks exhibiting a misorientation angle of 60º are observed resulting from the formation of mechanical twins inside grain Y with the initial <101> // TD fiber texture. By contrast, no detectable twin is observed by EBSD for the grain X with <001> orientation. The obtained results are similar to the texture evolution of TWIP steel during tensile test [42]. Experimental observations combined with the viscoplastic self-consistent model showed that <001> grains remain quite stable without interaction with neighboring orientations during uniaxial tensile straining. On the other hand, grains with <101> orientation are unstable and are reoriented towards <111> corner [42]. This also explains the texture evolution of the iHEA-V sample after fracture, where two dominant textures of <001> // TD and <113> // TD are observed (Fig. 10d). The final <001> // TD fiber texture results from the grains with an initial <001> orientation that are not rotated during uniaxial tensile straining. The <113> // TD fiber texture is evolved mainly due to the rotation of the grains with an orientation lying on the line connecting <001> and <101> poles. Assuming an fcc single crystal with the orientation, for example, close to <102>, slip initiates along the $[\bar{1}01]$ orientation on the (111) plane. With further straining, the slip direction of $[\bar{1}01]$ undergoes rotation towards the tensile axis. This rotation is depicted by shifting the initial orientation as the tensile axis towards $[\bar{1}01]$, until two slip systems with maximum Schmid factor on the line connecting <001> and <111> poles are activated. The rotation of the grains with the initial orientation close to <101> justifies the evolution towards the <113> // TD fiber texture in the deformed vertical sample.

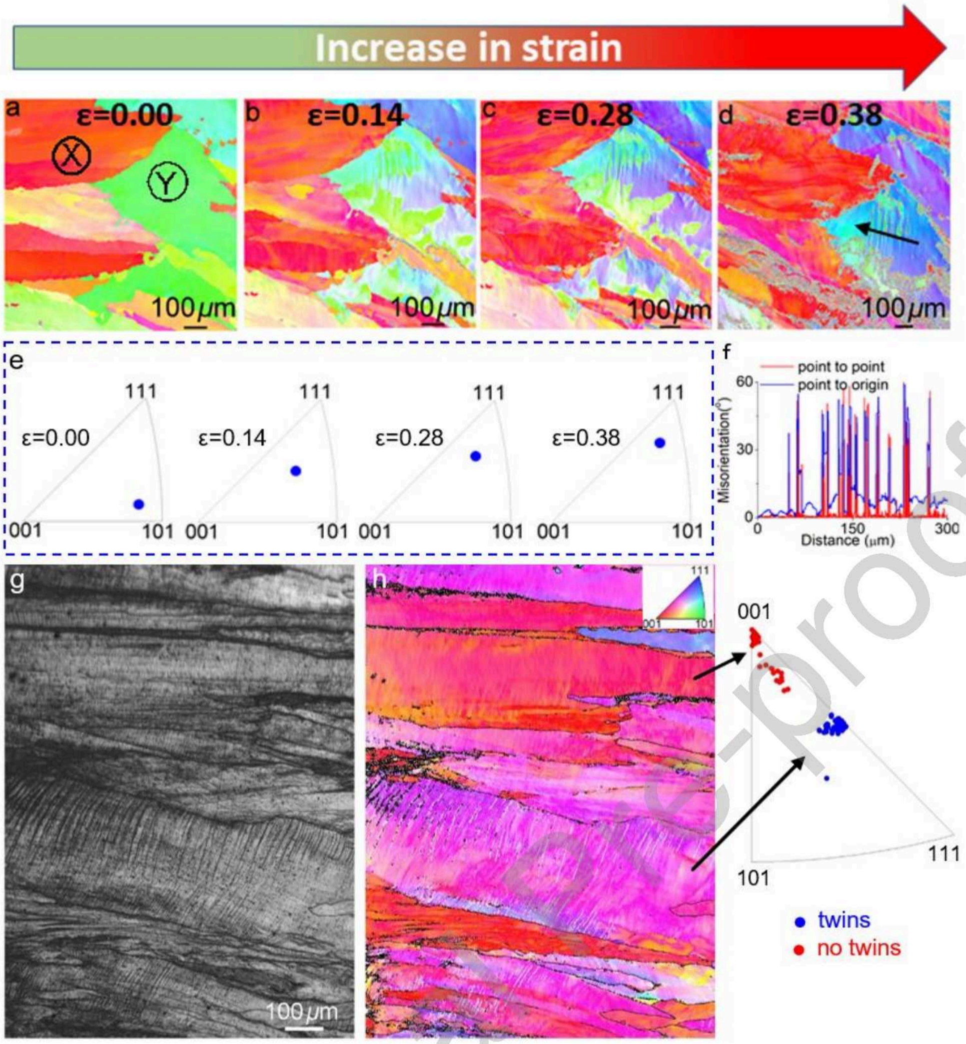

Fig. 14 (a-d) IPF maps showing the microstructural change in iHEA-V sample during tensile straining. (e) IPFs presenting the average misorientation of Y grain in (a) with respect to the TD. (f) Misorientation profile along the black arrow in (d). (g) IQ and (h) IPF maps of iHEA-V sample after tensile deformation.

The IQ and IPF maps of the fractured iHEA-V sample are shown in Fig. 14g and 14h, respectively. TBs are highlighted in white in Fig. 14h. Compared to the iHEA-H sample, the number and area fraction of mechanical twins decreased significantly. Moreover, the thickness of twins in the fractured iHEA-V sample is significantly smaller compared to the large band-shaped mechanical twins in the iHEA-H sample. Two groups of grains shown in Fig. 14h indicate that the grains with orientation close to <001> // TD are free of mechanical twins (red dots in IPF), whereas twins are activated inside the grains with orientation close to <113> // TD. In fact, these are the grains with an initial orientation of <102> // TD, which reorient during uniaxial tensile test.

The results obtained elucidate the orientation-dependent mechanical properties of the DEDed iHEA samples. The iHEA-H sample with dominant <111> // TD fiber texture is

Journal Pre-proof

deformed mainly by the formation of mechanical twins, whereas the iHEA-V sample with major <001> // TD shows very limited twining activity during tensile test. The maximum Schmid's factors for twinning and slip during tension and compression along <111> and <001> axes are presented in Table 3. In the case of the grains with <111> orientation parallel to TD, the Schmid's factor for twinning is higher than that for slip. The deformation characteristics observed in the case of iHEA-H sample complies well with the Schmid's law, where the grains are mostly deformed by the formation of mechanical twins during tensile testing. Multiple slip systems are activated inside these grains with low Schmid's factor for basal slip, leading to the dislocation pileup and reduction in effective stacking fault energy (SFE) and thus the formation of twinning [43]. By contrast, grains with <001> // TD have lower Schmid's factor for twinning compared with that of slip and thus are less favorable for mechanical twinning. As shown in Fig. 12 and Fig. 14, these grains are twin-free even after fracture and are most likely deformed via slip. Although Schmid's law explains the deformation characteristics of the tensile samples for two different directions, it basically applies to single crystals and does not account for the strain compatibility requirement with the neighboring grains in polycrystals [43]. Instead, the Taylor factor (M) can be used to justify the deformation mechanism of the microstructures with different textures. The Taylor factor distribution maps for the two samples before deformation are presented in Fig. 11b and d, which were plotted considering uniaxial tensile test and {111} <110> slip systems for an fcc structure. As shown, the iHEA-V sample with a dominant texture of <001> // TD has a lower Taylor factor compared to the iHEA-H sample with major texture of <111> // TD. The grains with <111> axis elongated towards TD or the ones that have rotated towards <111> pole (i.e. <101> // TD) have higher Taylor factor and are difficult to be deformed, which dissipate more deformation energy. Inside these grains, a higher dislocation density is generated to maintain the strain compatibility with adjacent grains, leading to a reduced effective SFE and thus promoting the formation of mechanical twins [44]. Similarly, in a recent study, Liu et al. [21] also reported crystallographic dependence of deformation twins in LMDed CoCrFeMnNi HEA. That is, deformation twins tended to occur in grains oriented close to the <111> // tensile direction, while the <001> texture did not show profuse deformation twins, which verifies the general notion that deformation-induced twins hardly appear in FCC metals with lower Taylor factor ($M < 2.6$) [43,45].

Journal Pre-proof

Table 3 Maximum Schmid's factor (*m*) for slip, twinning, leading and trailing partial dislocations in tension and compression.

Axis	Tensile				Compression			
	Slip	Twin	Leading partial	Trailing partial	Slip	Twin	Leading partial	Trailing partial
<111>	0.28	0.31	0.31	0.16	0.28	0.16	0.16	0.31
<001>	0.41	0.23	0.23	0.47	0.41	0.47	0.47	0.23

To further confirm the above deformation mechanisms that account for the excellent mechanical properties and remarkable anisotropy of the DEDed iHEA, TEM characterization was performed on the deformed grains with different orientations, namely near <001>, <111> and <113> // TD, respectively. The results are shown in Fig. 15-17. A large number of intersecting slip bands can be observed in the bright-field STEM image of the <001>-oriented grain as shown in Fig. 15a. The SAED pattern in Fig. 15a1 reveals a clear grain rotation near the slip band, while the SAED pattern in Fig. 15a2 shows a clear fcc single-crystal structure. Fig. 15b and d demonstrate the bright-field TEM observations of two well-defined slip bands. There is a high density of stacking faults (SFs) inside the slip band, and the HRTEM images in Fig. 15c and f provide close-up views of the SFs bundles. Fig. 15e displays intersecting SFs (marked with yellow arrows). Such dislocation pattern is typical for low-SFE alloys [46]. The interaction among SFs gliding on different {111} planes usually results in immobile Lomer-Cottrell (L-C) locks, which not only restrict the mobility of the SFs that generate them, but also serve as obstacles, further impeding the dislocation movement from the opposite direction [47], contributing to the enhancement of material strength. Previous studies have indicated that the combination of low SFE in HEAs and the rapid solidification during laser additive manufacturing process could notably influence the quantity and density of dislocations and SFs [48, 49], leading to the generation of SFs and L-C locks with high densities. Fig. 15g and h show enlarged views of the two precipitates marked in (a), which show no obvious shape changes after tensile testing, indicating the occurrence of an Orowan strengthening mechanism (will be discussed in the following content). Deformation twins were not detected in the deformed <001> // TD oriented grain, which was confirmed by the absence of twinning reflections in the SAED patterns (see insets in Fig. 15a and e). Therefore, it can be concluded that the gliding of dislocations along different slip planes constitutes the predominant deformation mechanism for the near <001> // TD oriented grains.

Journal Pre-proof

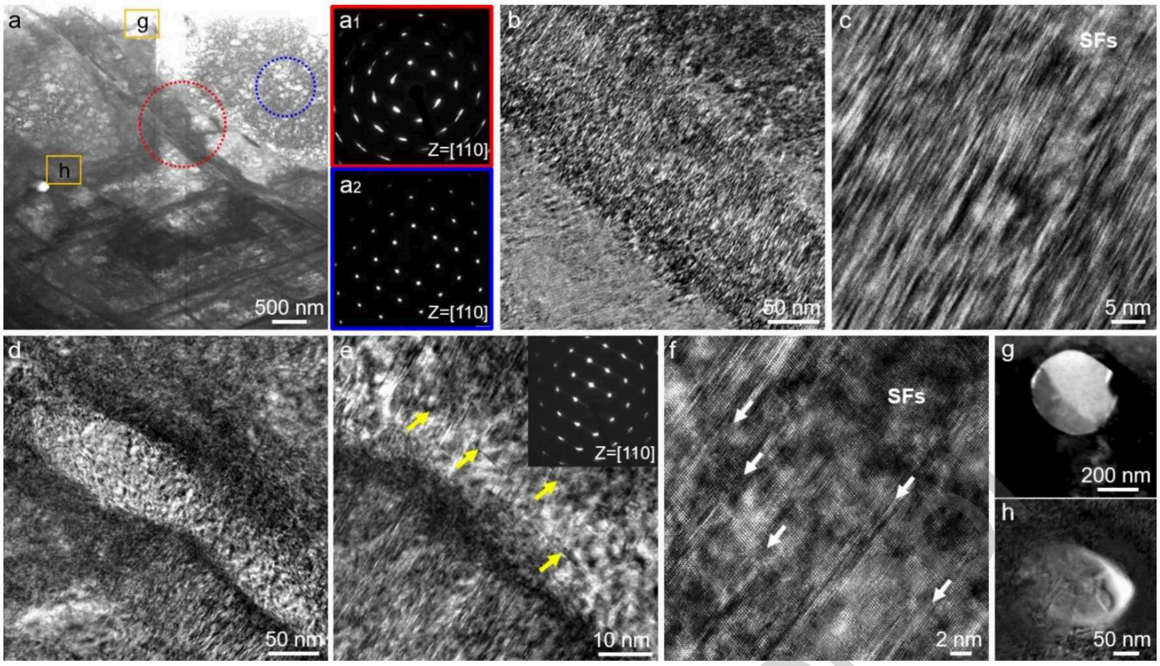

Fig. 15 Typical deformation microstructure of a near <001> // TD oriented grain: (a) STEM bright-field image with the corresponding SAED patterns, (b, d and e) TEM bright-field images of slip bands, (c, f) HRTEM images showing multiple SFs within the slip band in (b) and (d), respectively; (g, h) magnified view of precipitates marked in (a).

In contrast, high-density deformation twins are detected in the bright-field STEM image of the deformed <111> // TD oriented grain in Fig. 16a. Both primary and secondary twinning can be observed, as evidenced by the corresponding SAED patterns along the [110] zone axis in Fig. 16b. Dislocation entanglement can also be observed inside the twins due to the hindering effect of twin boundaries, which contributes to the increased strength. Fig. 16c is an enlarged view of the primary deformation twins, where multiple SFs can be observed at the twin interfaces. These SFs emerged from the interaction of partial dislocations within the fcc solid solution, serving as favored locations for the nucleation of deformation twins. Fig. 16d is an HRTEM image showing intersecting deformation twins and SFs. The misorientation angle between the primary and secondary twins is 70.5°, consistent with previously reported results for fcc-structured HEA single crystals [50]. Fig. 16e and f show the HRTEM images of the primary and secondary twins, respectively, providing a more detailed view of the deformation twins with some extrinsic SFs detected at the fcc matrix and twin boundaries. The average twinning spacing is comparable in both twin variants. In addition, it can also be observed from Fig. 16a that the intersecting twins create additional immobile L-C locks, which subdivides the matrix into smaller blocks, achieving a dynamic grain refinement effect [46]. These outcomes highlight a more prominent role of deformation twinning and partial dislocation slip mechanisms within <111> // TD oriented grains.

Journal Pre-proof

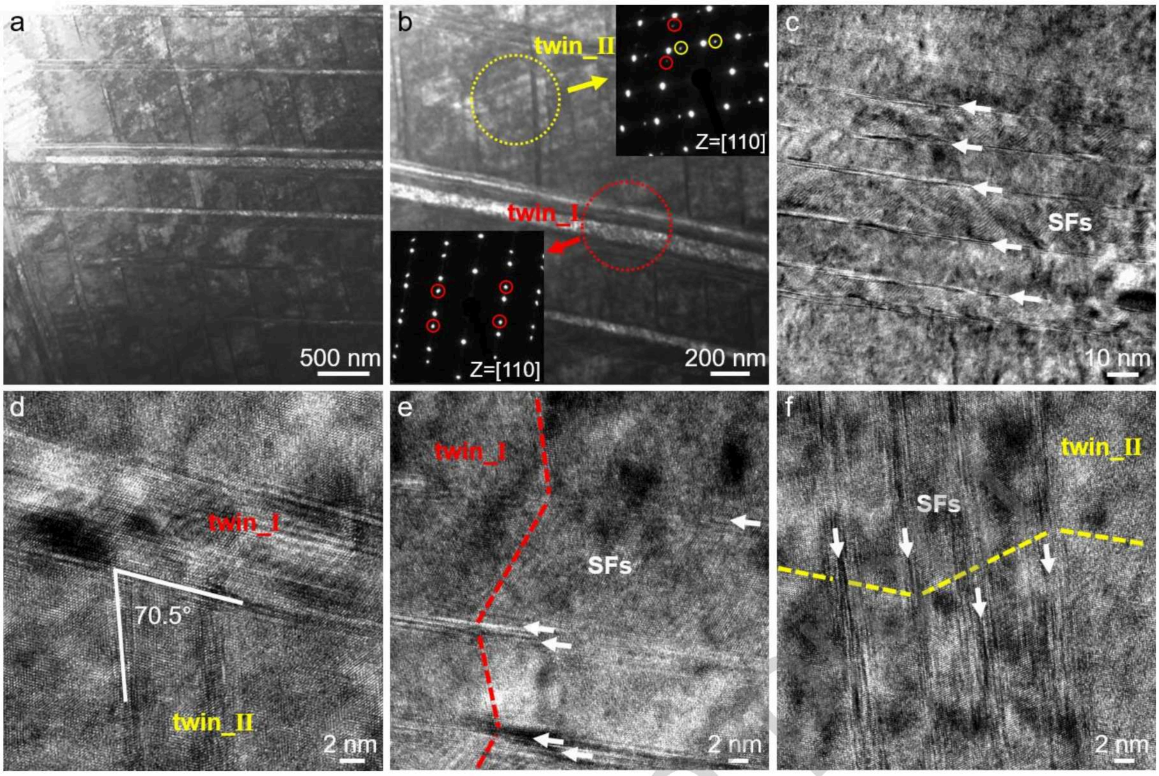

Fig. 16 Typical deformation microstructure of a near <111> oriented grain: (a) and (b) STEM bright-field image with the corresponding SAED patterns, showing a high density of twins, (c) TEM bright-field image of primary deformation twins, (d) HRTEM image showing the intersecting primary and secondary twins, (e) and (f) HRTEM images showing primary and secondary twins, respectively.

For the <113> // TD oriented deformed grain in Fig. 17, slip bands and deformation twins can be observed simultaneously, whereas the size of the deformation twins is significantly reduced compared to the <111> grains. Fig. 17b shows the bright-field TEM image of the slip band, and the corresponding SAED pattern reveals an obvious grain rotation near the slip band. The SAED patterns of two different regions in Fig. 17a also confirm the grain rotation on both sides of the slip band in the deformed grain. Similarly, a high density of SFs can be detected within the slip band in Fig. 17b, and the corresponding HRTEM image is shown in Fig. 17c. The presence of deformation twins can be confirmed by the bright-field TEM image and its corresponding SAED pattern in Fig. 17d. A large number of intersecting SFs along two {111} slip planes can also be observed around the nanotwins, which act as favored sites for the initiation of twinning systems. The formation of deformation twins is less prevalent in deformed <113> grains compared with that in deformed <111> grains. Fig. 17e and f show HRTEM images of two twin variants, confirming that SFs are widely distributed around the deformation twins. Notably, the thickness of the secondary twins observed in Fig. 16f is only a few atomic layers, so no obvious secondary twin spots are detected in the SAED pattern shown in the insert of Fig. 17d.

Journal Pre-proof

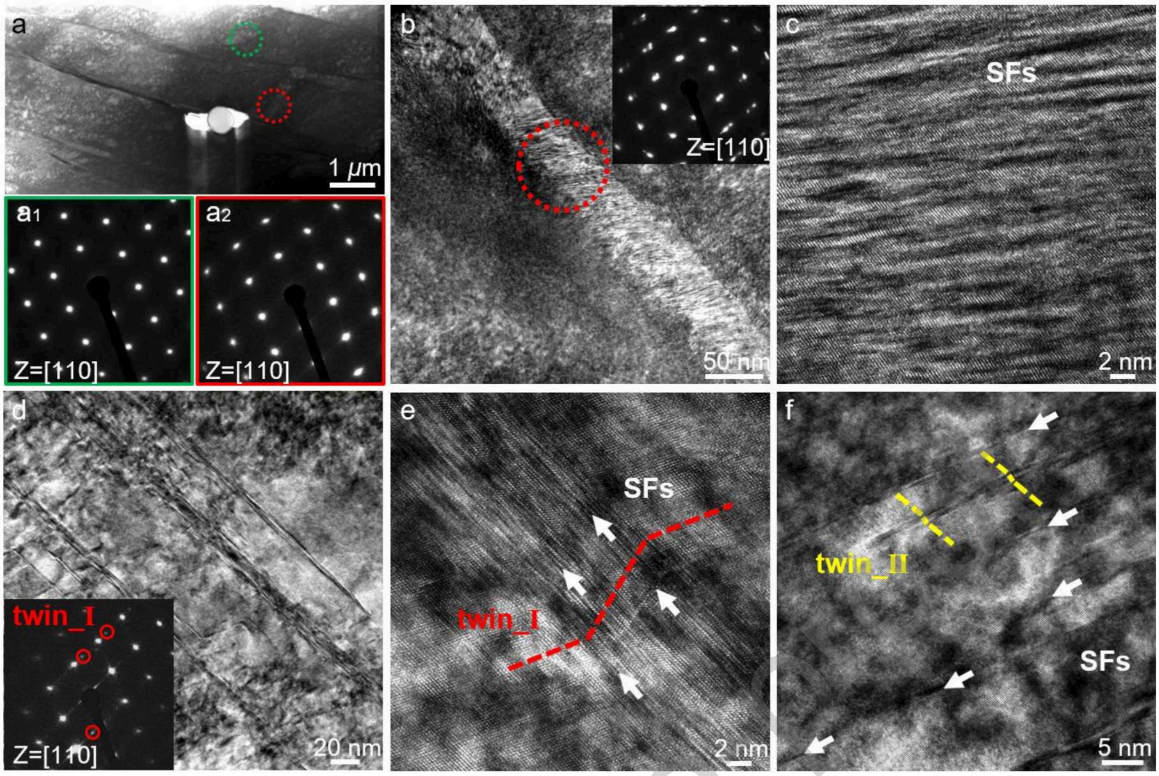

Fig. 17 Typical deformation microstructure of a near <113> oriented grain: (a) STEM bright-field image with the corresponding SAED patterns, (b) TEM bright-field image of a slip band with an inserted corresponding SAED pattern, (c) HRTEM image showing multiple SFs within the slip band in (b), (d) TEM bright-field image with the corresponding SAED pattern showing the formation of primary twins, (e, f) HRTEM images displaying primary and secondary twins, respectively.

Moreover, a spherical precipitate with the size of about 500 nm can be seen in Fig. 17a. While undergoing interaction with the strain field upon loading, the precipitates led to the formation of micro-voids along the slip directions. Specifically, two triangular spacings situated on opposite sides of the slip band surrounding the precipitate are generated, which has also been reported in [51], indicating a strengthening contribution from the Orowan strengthening mechanism. This precipitation strengthening can be elucidated by the creation of dislocation loops. For incoherent, robust precipitates that dislocations cannot penetrable, dislocations are promoted to circumvent the precipitates via the Orowan mechanism [52]. Thus, once Orowan loops are formed, the dislocations necessitate added stress to bypass the precipitates, consequently leading to an increased strain hardening rate. The contribution from Orowan strengthening was reported to account for 44% of all strengthening contributions of additively manufactured oxide-dispersion strengthened CoCrFeMnNi HEAs [51]. Similar results have also been reported by Kim et al. [53], where the calculated contribution from Orowan strengthening was 44% after compression tests on LPBFed CoCrFeMnNi HEA. Accordingly, the strengthening contribution from oxide nanoparticles in the current study is

Journal Pre-proof

estimated using the Orowan strengthening model, which can be evaluated according to the equation [54]:

$$\tau = Gb(L - d)$$

where G is the shear modulus of the iHEA (81 GPa [55]), b is the Burgers vector (0.255 nm [55]), d is the average diameter of the nanoparticles, and L is the average distance between nanoparticles that can be expressed as follows [51, 53]:

$$L = \sqrt{\frac{2}{3}}d(\sqrt{\frac{\pi}{4v}} - 1),$$

where v is the volume fraction of the oxide nanoparticles. The d (397 nm) and v (0.42%) are measured via ImageJ using Fig. 4c. By using these two equations, the estimated strengthening contribution is τ = 83 MPa, which accounts for approximately 19% and 11% for the yield strength of current iHEA-H and iHEA-V samples, respectively. Although significantly lower than the Orowan strengthening contribution mentioned in [51, 53], Mn-rich oxides still play a key role in achieving the superior mechanical properties of additively manufactured HEAs.

Furthermore, for the current DED-processed iHEA, the nano-scale $M_{23}C_6$/M_7C_6 carbides distributed at the cellular boundaries (Fig. 6b) can also effectively hinder the dislocation movement and generate high back stress-induced hardening through profuse geometrically necessary dislocations (GNDs) during plastic deformation, further strengthening this alloy [56, 57]. Specifically, GNDs would be generated during plastic deformation to maintain physical continuity at the interfaces. In the materials with heterostructures, the GNDs can evolve more actively at the interface between hard and soft domains [57-59]. For the current iHEA, since the carbides are significantly stronger than the soft FCC matrix, the FCC matrix would sustain higher plastic strain during plastic deformation, resulting in a localized strain gradient near the interface between the matrix and carbides. GNDs are then generated and piled up at the interface to accommodate the strain gradient, producing back stress induced hardening, which contributes to the enhanced stress levels and strain hardening ability. On the other hand, these carbides have been reported to block dislocation more effectively than cellular boundaries [57], suggesting that the volume fraction of carbides can be an important factor for modulating the mechanical properties of C-containing HEAs.

It is worthwhile to note that unlike previous reports [11,19,20], no TRIP effect was observed upon tensile loading in the current study. High-energy SXRD analysis was performed on the fractured samples in both orientations, as shown in Fig. 18, which confirms the absence of phase transformation during deformation. This can be attributed to the slight deviation of the powder composition of the current iHEA from the nominal composition

(Table 1). Slightly higher Mn content increases the free energy difference between fcc and hcp ($\Delta G^{FCC \rightarrow HCP}$) and hence the stability of the fcc phase [60]. Higher carbon content also increases the SFE of the iHEA and changes the deformation mechanism from TRIP to TWIP. Therefore, an accurate tuning of the composition is required in order to trigger both TWIP and TRIP mechanisms. Besides, the DED process was carried out in the open air without Ar gas protection, which may lead to the nitrogen penetration into the melt pool and thus into the as-deposited structure. Recently, Zhang et al. [61] studied the co-doping of carbon and nitrogen into the $Fe_{49.5}Mn_{30}Cr_{10}Co_{10}$ and reported that the nitrogen addition increased the phase stability and SFE, avoiding the TRIP effect upon tensile loading. In addition, according to Park et al. [62], LPBF-produced $(CoCrFeMnNi)_{99}C_1$ HEA exhibited the formation of mechanical twins within the coarse grains of the deformed sample, suggesting an inverse correlation between grain size and critical twin stress. Thus, the large grain size in the current DEDed iHEA may suppress the hcp phase nucleation but favor the twinning nucleation during straining. Another factor that needs to be mentioned is the influence of cellular/ substructure on the TRIP effect. Karthik et al. [63] pointed out that the cellular substructure decorated with dislocations significantly improves the mechanical stability of the austenite of AM316L and delays the deformation-induced martensitic transformation at low temperature (77 K). They believe that if austenite grains have a higher dislocation density, the movement of Shockley partial dislocations will require additional energy to bypass the dislocation tangles already present in the material, making the austenite more stable. On the contrary, in another recent study, Kim et al. [64] proposed that the cellular substructure with elemental segregation in AM304L may locally lower the SFE and promote the transformation of fine and homogeneous martensite, which can mitigate the local stress concentration during plastic deformation and induce uniform plastic deformation, thereby promoting the TRIP effect [65]. These opposing views still require further in-depth research. Generally, during deformation, the TRIP effect can substantially enhance mechanical strength while maintaining an acceptable total elongation range. By contrast, the TWIP effect exhibits an average mechanical strength but remarkable deformation at fracture [52].

Journal Pre-proof

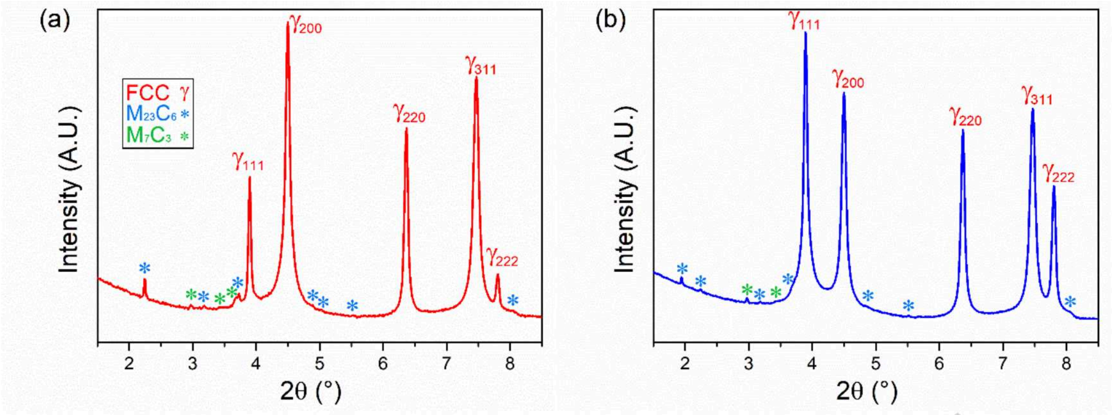

Fig. 18. High-energy SXRD patterns of (a) iHEA-H and (b) iHEA-V samples after tensile deformation.

3.3 Micro-pillar compression

The orientation-dependent deformation mechanism of the DEDed iHEA was also evaluated by micro-pillar compression tests. The Schmid's factors for twinning and slip concerning two different compression axes are listed in Table 3. The compression stress-strain curves for the micro-pillars along [001] and [111] orientations are shown in Fig. 19a and 19b, respectively. Distinct differences are observed in the plastic behavior of the two micro-pillars. According to the Schmid's factor in Table 3, compression along the [001] axis promoted the activation of mechanical twinning, while the [111] orientation is recognized for its engagement of multiple slip systems upon compression. As shown in Fig. 19a, compression along the [001] axis is associated with large strain bursts followed by a sharp drop in stress. By contrast, the [111] orientation that favors dislocation glide shows a continuous work hardening with very small strain bursts. The transition from elastic to plastic region of the [001] orientation is accompanied by a sudden drop in load, whereas the [111] oriented pillar shows continuous and smooth yielding after the elastic region. The yield onset was characterized as the point where the linear elastic part shifts to the non-linear plastic part. The micro-pillar compression test results are summarized in Table 4. Compression along [001] axis shows a slightly higher average yield strength compared with the [111] orientation. The critical resolved shear stress (CRSS) was calculated using $\tau_{CRSS} = m \cdot \sigma_y$. The yield stress from the [001] and [111] compression tests were used to calculate the CRSS for twinning and slip, respectively. The results obtained in Table 4 propose higher CRSS for twining (290 ± 38 MPa) than slip (148 ± 45 MPa). Karaman et al. [66] also reported higher CRSS for twining compared to slip in the bulk single crystal compression of Hadfield steel. Comparable findings were also reported in the micro-pillar compression of TWIP steel [67]. The representative SEM images of the deformed micro-pillars for [001] and [111] orientations are

Journal Pre-proof

shown in Fig. 19c and d, respectively. The deformed [001] micro-pillar, which is favored for twining, is characterized by the formation of thick shear-type steps, while the deformed [111] micro-pillar oriented for slip deformation shows narrow shear bands indicative slip lines. The difference in deformation mechanism for the two micro-pillars are explained well with the Schmid's factors in Table 3. Slip deformation in fcc materials on {111} <110> system is carried out by the formation of glissile partial Shockley dislocations. The leading partial dislocation initiates the formation of a stacking fault, while the trailing partial closes the generated stacking fault [68]. For the compression along [111] orientation, the Schmid's factor for the trailing partial surpasses that of the leading partial. This yields a greater resolved shear stress on the trailing partial, enabling it to close the stacking fault. This results in perfect dislocation slip for [111] micro-pillar compression. In contrast, when compressing along the [001] axis, the Schmid's factor for the leading partial is larger, causing the trailing partial is not able to close the stacking fault. This leads to the generation of wide stacking fault and mechanical twins. The work hardening rate (WHR) for the two oriented micro-pillars were calculated from the onset of yielding until 10% deformation ($WHR_{y\rightarrow10\%}$). As presented in Table 4, the initial $WHR_{y\rightarrow10\%}$ for the [111] orientation with multiple activated slip systems is much higher than that of the [001] orientation which favored twinning. In fact, compression along the [111] axis leads to a continuous WHR through deformation. The results obtained from micro-pillar compression can explain the comparable WHRs of the iHEA-V and iHEA-H sample, despite the fact that much less mechanical twins were activated during tensile deformation of the iHEA-V sample (Fig. 7b). Wang et al. [67] studied the work hardening behavior of TWIP steel during micro-pillar compression test and showed higher WHR for the pillars deformed via perfect dislocation glide. Laing et al. [69] analyzed the contribution of dislocations and twins to the work hardening of a TWIP steel and reported that dislocations account for 90% of the incremental increase in load after yielding.

Journal Pre-proof

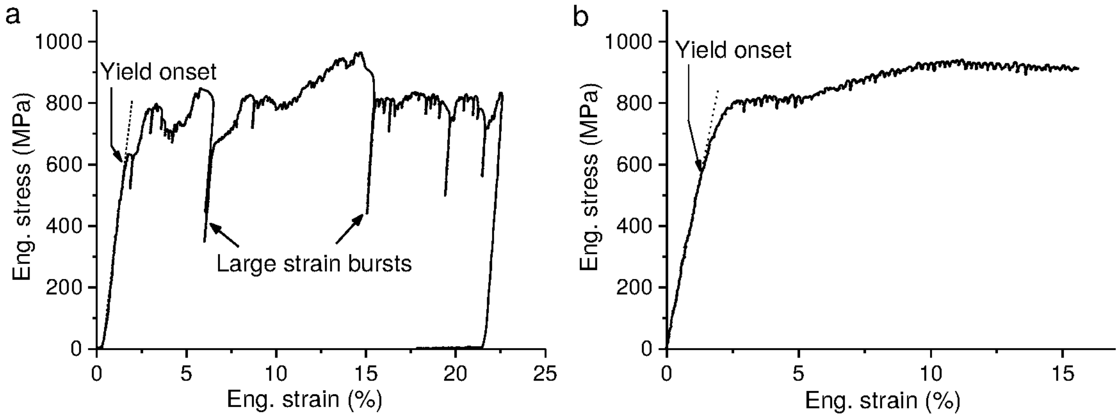

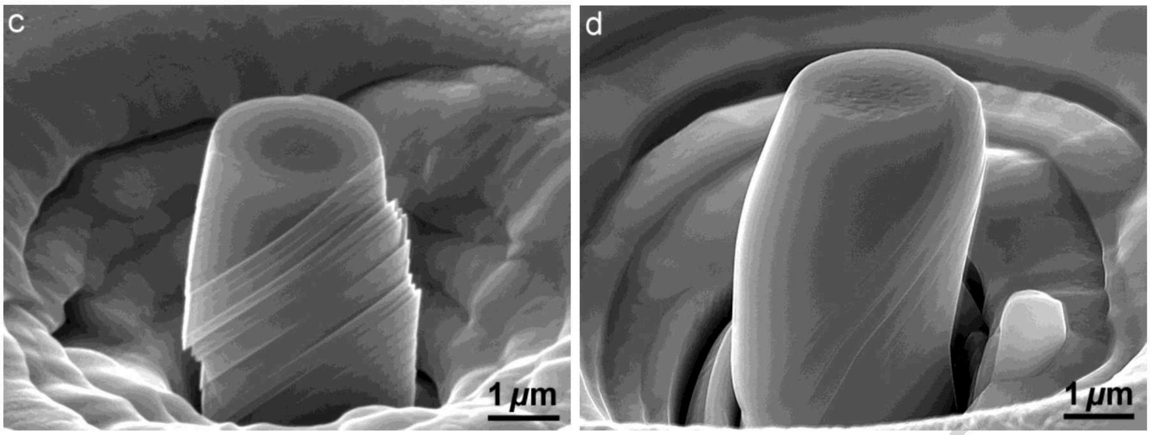

Fig. 19 Stress-strain curves of the micro-pillar compression tests along (a) [001] and (b) [111] orientations, (c) and (d) the corresponding SEM images of deformed micro-pillars.

Table 4 Summary of the micro-pillar compression test results.

Pillar	Deformation mode	Yield strength, σ_y (MPa)	CRSS for slip, τ_{slip} (MPa)	CRSS for twin, τ_{twin} (MPa)	$WHR_{y \to 10\%}$ (MPa)
[001]	Twin	625 ± 70		290 ± 38	2091
[111]	Multiple slip system	563 ± 98	148 ± 45		4198

4. Conclusions

In summary, $Fe_{49.5}Mn_{30}Cr_{10}Co_{10}C_{0.5}$ iHEA was successfully fabricated using laser directed energy deposition (DED). The microstructure, orientation-dependent mechanical properties, strengthening and deformation mechanisms of as-deposited iHEA samples were systematically investigated using multiscale characterization approaches including EBSD, SEM, SXRD, (S)TEM and mechanical testing. The main conclusions are as follows:

(1) The DED-built iHEA sample exhibited a dominant fcc phase with [001] and [101] crystallographic texture along the deposition direction, and the formation of $M_{23}C_6$ and M_7C_3 carbides was also detected. The microstructural features including epitaxially grown elongated grains, equiaxed and columnar dendritic structures, and elemental segregation at subgrain boundaries were observed.

(2) The as-deposited iHEA shows an excellent synergy of strength and ductility. The ultimate tensile strength and elongation of iHEA-H and iHEA-V samples reached 1000 MPa and 36%, 750 MPa and 52%, respectively, pushing the boundaries of the tensile properties and outperforming other HEAs produced by the DED method. The orientation dependence of the deformation response of iHEA revealed that for the iHEA-H sample with strong <111> // tensile direction (TD) fiber texture, the microstructure is severely deformed via the formation

Journal Pre-proof

of mechanical twins. By contrast, the iHEA-V sample with the <001> // TD dominant texture shows less deformation-induced twining activity and is mainly deformed via slip.

(3) Nanoscale carbides and Mn-rich oxides distributed at cellular boundaries can also effectively hinder dislocation movement, produce high back stress-induced hardening and precipitation strengthening, and play a key role in achieving the excellent mechanical properties of additively manufactured iHEA.

(4) The single crystal micro-pillar compression testing revealed that the deformation mechanism complies well with the Schmid's factor, and a higher critical resolved shear stress for twining compared to that for slip was confirmed.

Declaration of Competing Interest

The authors declare that they have no known competing financial interests or personal relationships that could have appeared to influence the work reported in this paper.

Acknowledgment

This research was carried out under project number S17024o in the framework of the Partnership Program of the Materials innovation institute M2i (www.m2i.nl) and the Netherlands Organization for Scientific Research (www.nwo.nl).

WZ acknowledges the China Scholarship Council for her PhD grant (CSC No. 201906250212). YP acknowledges financial support by Samenwerkingsverband Noord-Nederland (SNN) within the program "3D Print Kompas". JPO and JS acknowledge Fundação para a Ciência e a Tecnologia (FCT - MCTES) for its financial support via the project UID/00667/2020 (UNIDEMI). JPO acknowledges funding by national funds from FCT - Fundação para a Ciência e a Tecnologia, I.P., in the scope of the projects LA/P/0037/2020, UIDP/50025/2020 and UIDB/50025/2020 of the Associate Laboratory Institute of Nanostructures, Nanomodelling and Nanofabrication – i3N. JS acknowledges the China Scholarship Council for her PhD grant (CSC No. 201808320394). The authors acknowledge DESY (Hamburg, Germany), a member of the Helmholtz Association HGF, for the provision of experimental facilities. Beamtime was allocated for proposal I-20210899 EC. The research leading to this result has been supported by the project CALIPSOplus under the Grant Agreement 730872 from the EU Framework Programme for Research and Innovation HORIZON 2020. SF acknowledges financial support by the National Natural Science Foundation of China (No. 52105318) and Fundamental Research Funds for the Central Universities (Youth Teacher International Exchange & Growth Program No. QNXM20220027).

Journal Pre-proof

Journal Pre-proof

References

[1] D.B. Miracle, O.N. Senkov, A critical review of high entropy alloys and related concepts, Acta Mater. 122 (2017) 448–511.

[2] E.J. Pickering, N.G. Jones, High-entropy alloys: a critical assessment of their founding principles and future prospects, Int. Mater. Rev. 61 (2016) 183–202.

[3] Y. Zhang, T.T. Zuo, Z. Tang, M.C. Gao, K.A. Dahmen, P.K. Liaw, Z.P. Lu, Microstructures and properties of high-entropy alloys, Prog. Mater. Sci. 61 (2014) 1–93.

[4] J.W. Yeh, S.K. Chen, S.J. Lin, J.Y. Gan, T.S. Chin, T.T. Shun, C.H. Tsau, S.Y. Chang, Nanostructured high-entropy alloys with multiple principal elements: Novel alloy design concepts and outcomes, Adv. Eng. Mater. 6 (2004) 299–303.

[5] F. Otto, A. Dlouhý, K.G. Pradeep, M. Kuběnová, D. Raabe, G. Eggeler, E.P. George, Decomposition of the single-phase high-entropy alloy CrMnFeCoNi after prolonged anneals at intermediate temperatures, Acta Mater. 112 (2016) 40–52.

[6] F. Otto, Y. Yang, H. Bei, E.P. George, Relative effects of enthalpy and entropy on the phase stability of equiatomic high-entropy alloys, Acta Mater. 61 (2013) 2628–2638.

[7] M.J. Yao, K.G. Pradeep, C.C. Tasan, D. Raabe, A novel, single phase, non-equiatomic FeMnNiCoCr high-entropy alloy with exceptional phase stability and tensile ductility, Scr. Mater. 72–73 (2014) 5–8.

[8] Z. Lei, X. Liu, Y. Wu, H. Wang, S. Jiang, S. Wang, X. Hui, Y. Wu, B. Gault, P. Kontis, D. Raabe, L. Gu, Q. Zhang, H. Chen, H. Wang, J. Liu, K. An, Q. Zeng, T.-G. Nieh, Z. Lu, Enhanced strength and ductility in a high-entropy alloy via ordered oxygen complexes, Nature. 563 (2018) 546–550.

[9] Z. Wu, C.M. Parish, H. Bei, Nano-twin mediated plasticity in carbon-containing FeNiCoCrMn high entropy alloys, J. Alloys Compd. 647 (2015) 815–822.

[10] J.B. Seol, J.W. Bae, Z. Li, J. Chan Han, J.G. Kim, D. Raabe, H.S. Kim, Boron doped ultrastrong and ductile high-entropy alloys, Acta Mater. 151 (2018) 366–376.

[11] Z. Li, C.C. Tasan, H. Springer, B. Gault, D. Raabe, Interstitial atoms enable joint twinning and transformation induced plasticity in strong and ductile high-entropy alloys, Sci. Rep. 7 (2017) 40704.

[12] M. Wang, Z. Li, D. Raabe, In-situ SEM observation of phase transformation and twinning mechanisms in an interstitial high-entropy alloy, Acta Mater. 147 (2018) 236–246.

[13] D. Lin, L. Xu, X. Li, H. Jing, G. Qin, H. Pang, F. Minami, A Si-containing FeCoCrNi high-entropy alloy with high strength and ductility synthesized in situ via selective laser melting, Addit. Manuf. 35 (2020) 101340.

[14] T. Borkar, B. Gwalani, D. Choudhuri, C. V Mikler, C.J. Yannetta, X. Chen, R. V Ramanujan, M.J. Styles, M.A. Gibson, R. Banerjee, A combinatorial assessment of $Al_xCrCuFeNi_2$ ($0 < x < 1.5$) complex concentrated alloys: Microstructure, microhardness, and magnetic properties, Acta Mater. 116 (2016) 63–76.

[15] S. Xiang, H. Luan, J. Wu, K.-F. Yao, J. Li, X. Liu, Y. Tian, W. Mao, H. Bai, G. Le, Q. Li,

Microstructures and mechanical properties of CrMnFeCoNi high entropy alloys fabricated using laser metal deposition technique, J. Alloys Compd. 773 (2019) 387–392.

[16] P. Agrawal, S. Thapliyal, S.S. Nene, R.S. Mishra, B.A. McWilliams, K.C. Cho, Excellent strength-ductility synergy in metastable high entropy alloy by laser powder bed additive manufacturing, Addit. Manuf. 32 (2020) 101098.

[17] C. Haase, F. Tang, M.B. Wilms, A. Weisheit, B. Hallstedt, Combining thermodynamic modeling and 3D printing of elemental powder blends for high-throughput investigation of high-entropy alloys – Towards rapid alloy screening and design, Mater. Sci. Eng. A 688 (2017) 180–189.

[18] Y. Chew, G.J. Bi, Z.G. Zhu, F.L. Ng, F. Weng, S.B. Liu, S.M.L. Nai, B.Y. Lee, Microstructure and enhanced strength of laser aided additive manufactured CoCrFeNiMn high entropy alloy, Mater. Sci. Eng. A. 744 (2019) 137–144.

[19] Z.G. Zhu, X.H. An, W.J. Lu, Z.M. Li, F.L. Ng, X.Z. Liao, U. Ramamurty, S.M.L. Nai, J. Wei, Selective laser melting enabling the hierarchically heterogeneous microstructure and excellent mechanical properties in an interstitial solute strengthened high entropy alloy, Mater. Res. Lett. 7 (2019) 453–459.

[20] Y. Chew, Z.G. Zhu, F. Weng, S.B. Gao, F.L. Ng, B.Y. Lee, G.J. Bi, Microstructure and mechanical behavior of laser aided additive manufactured low carbon interstitial $Fe_{49.5}Mn_{30}Co_{10}Cr_{10}C_{0.5}$ multicomponent alloy, J. Mater. Sci. Technol. 77 (2021) 38–46.

[21] Y. Liu, J. Ren, S. Guan, C. Li, Y. Zhang, S. Muskeri, Z. Liu, D. Yu, Y. Chen, K. An, Y. Cao, W. Liu, Y. Zhu, W. Chen, S. Mukherjee, T. Zhu, W. Chen, Microstructure and mechanical behavior of additively manufactured CoCrFeMnNi high-entropy alloys: Laser directed energy deposition versus powder bed fusion, Acta Mater. 250 (2023) 118884.

[22] M.-S. Pham, B. Dovgyy, P.A. Hooper, C.M. Gourlay, A. Piglione, The role of side-branching in microstructure development in laser powder-bed fusion, Nat. Commun. 11 (1) (2020) 749.

[23] L. Thijs, M.L. Montero Sistiaga, R. Wauthle, Q. Xie, J.-P. Kruth, J. Van Humbeeck, Strong morphological and crystallographic texture and resulting yield strength anisotropy in selective laser melted tantalum, Acta Mater. 61 (12) (2013) 4657–4668.

[24] T. DebRoy, H.L. Wei, J.S. Zuback, T. Mukherjee, J.W. Elmer, J.O. Milewski, A.M. Beese, A. Wilson-Heid, A. De, W. Zhang, Additive manufacturing of metallic components – process, structure and properties, Prog. Mater. Sci. 92 (2018) 112–224.

[25] M. Jin, A. Piglione, B. Dovgyy, E. Hosseini, P.A. Hooper, S.R. Holdsworth, M.-S. Pham, Cyclic plasticity and fatigue damage of CrMnFeCoNi high entropy alloy fabricated by laser powder-bed fusion, Addit. Manuf. 36 (2020) 101584.

[26] Z. Tong, X. Ren, J. Jiao, W. Zhou, Y. Ren, Y. Ye, E.A. Larson, J. Gu, Laser additive manufacturing of FeCrCoMnNi high-entropy alloy: Effect of heat treatment on microstructure, residual stress and mechanical property, J. Alloys Compd. 785 (2019) 1144–1159.

[27] M. Laurent-Brocq, A. Akhatova, L. Perrière, S. Chebini, X. Sauvage, E. Leroy, Y. Champion, Insights into the phase diagram of the CrMnFeCoNi high entropy alloy, Acta Mater. 88 (2015) 355–365.

[28] F. Kies, P. Köhnen, M.B. Wilms, F. Brasche, K.G. Pradeep, A. Schwedt, S. Richter, A. Weisheit, J.H. Schleifenbaum, C. Haase, Design of high-manganese steels for additive manufacturing

Journal Pre-proof

applications with energy-absorption functionality, Mater. Des. 160 (2018) 1250–1264.

[29] J.G. Kim, J.M. Park, J.B. Seol, J. Choe, J.-H. Yu, S. Yang, H.S. Kim, Nano-scale solute heterogeneities in the ultrastrong selectively laser melted carbon-doped CoCrFeMnNi alloy, Mater. Sci. Eng. A 773 (2020) 138726.

[30] X. Gao, Z. Yu, W. Hu, Y. Lu, Z. Zhu, Y. Ji, Y. Lu, Z. Qin, X. Lu, In situ strengthening of CrMnFeCoNi high-entropy alloy with Al realized by laser additive manufacturing, J. Alloys Compd. 847 (2020), Article 156563

[31] J. Joseph, P. Hodgson, T. Jarvis, X. Wu, N. Stanford, D.M. Fabijanic, Effect of hot isostatic pressing on the microstructure and mechanical properties of additive manufactured AlxCoCrFeNi high entropy alloys, Mater. Sci. Eng. A 733 (2018) 59–70

[32] S. Zhao, D. Xin, X. Chen, J. Stasic, M. Trtica, A.N. Siddiquee, S. Mohan, Microstructure and enhanced tensile properties of AlCoxCrFeNi high entropy alloys with high Co content fabricated by laser melting deposition, J. Alloys Compd. 917 (2022) 165403.

[33] P. Niu, R. Li, Z. Fan, T. Yuan, Z. Zhang, Additive manufacturing of TRIP-assisted dual-phases Fe50Mn30Co10Cr10 high-entropy alloy: Microstructure evolution, mechanical properties and deformation mechanisms, Mater. Sci. Eng. A 814 (2021) 141264.

[34] M.A. Melia, J.D. Carroll, S.R. Whetten, S.N. Esmaeely, J. Locke, E. White, I. Anderson, M. Chandross, J.R. Michael, N. Argibay, E.J. Schindelholz, A.B. Kustas, Mechanical and corrosion properties of additively manufactured CoCrFeMnNi high entropy alloy, Addit. Manuf. 29 (2019) 100833.

[35] X. Zhang, R. Li, L. Huang, A. Amar, C. Wu, G. Le, X. Liu, D. Guan, G. Yang, J. Li, Influence of in-situ and ex-situ precipitations on microstructure and mechanical properties of additive manufacturing CoCrFeMnNi high-entropy alloys, Vacuum 187 (2021) 110111.

[36] Y. Bai, H. Jiang, K. Yan, M. Li, Y. Wei, K. Zhang, B. Wei, Phase transition and heterogeneous strengthening mechanism in CoCrFeNiMn high-entropy alloy fabricated by laser-engineered net shaping via annealing at intermediate-temperature, J. Mater. Sci. Technol. 92 (2021) 129–137.

[37] J. Li, S. Xiang, H. Luan, A. Amar, X. Liu, S. Lu, Y. Zeng, G. Le, X. Wang, F. Qu, C. Jiang, G. Yang, Additive manufacturing of high-strength CrMnFeCoNi high-entropy alloys-based composites with WC addition, J. Mater. Sci. Technol. 35 (2019) 2430–2434.

[38] Q. Wang, A. Amar, C. Jiang, H. Luan, S. Zhao, H. Zhang, G. Le, X. Liu, X. Wang, X. Yang, J. Li, CoCrFeNiMo0.2 high entropy alloy by laser melting deposition: Prospective material for low temperature and corrosion resistant applications, Intermetallics 119 (2020) 106727.

[39] K. Zhou, J. Li, L. Wang, H. Yang, Z. Wang, J. Wang, Direct laser deposited bulk $CoCrFeNiNb_x$ high entropy alloys, Intermetallics 114 (2019) 106592.

[40] L. Huang, Y. Sun, A. Amar, C. Wu, X. Liu, G. Le, X. Wang, J. Wu, K. Li, C. Jiang, J. Li, Microstructure evolution and mechanical properties of AlCoCrFeNi high-entropy alloys by laser melting deposition, Vacuum 183 (2021) 109875.

[41] D. Barbier, N. Gey, S. Allain, N. Bozzolo, M. Humbert, Analysis of the tensile behavior of a TWIP steel based on the texture and microstructure evolutions, Mater. Sci. Eng. A 500 (2009) 196–206.

[42] A.A. Saleh, E. V Pereloma, A.A. Gazder, Microstructure and texture evolution in a twinning-

Journal Pre-proof

induced-plasticity steel during uniaxial tension, Acta Mater. 61 (2013) 2671–2691.

[43] H. Beladi, I.B. Timokhina, Y. Estrin, J. Kim, B.C. De Cooman, S.K. Kim, Orientation dependence of twinning and strain hardening behaviour of a high manganese twinning induced plasticity steel with polycrystalline structure, Acta Mater. 59 (2011) 7787–7799.

[44] J.J. Jonas, L.S. Tóth, Modelling oriented nucleation and selective growth during dynamic recrystallization, Scr. Metall. Mater. 27 (1992) 1575–1580.

[45] X. Wang, J.A. Muñiz-Lerma, M.Attarian Shandiz, O. Sanchez-Mata, M. Brochu, Crystallographic-orientation-dependent tensile behaviours of stainless steel 316L fabricated by laser powder bed fusion, Mater. Sci. Eng. A 766 (2019) 138395.

[46] N. Yao, T. Lu, K. Feng, B. Sun, R.Z. Wang, J. Wang, Y. Xie, P. Zhao, B. Han, X.C. Zhang, S.T. Tu, Ultrastrong and ductile additively manufactured precipitation-hardening medium-entropy alloy at ambient and cryogenic temperatures, Acta Mater. 236 (2022) 118142.

[47] D.D. Zhang, J.Y. Zhang, J. Kuang, G. Liu, J. Sun, Superior strength-ductility synergy and strain hardenability of Al/Ta co-doped NiCoCr twinned medium entropy alloy for cryogenic applications, Acta Mater. 220 (2021) 117288 .

[48] Z. Xu, H. Zhang, X. Du, Y. He, H. Luo, G. Song, L. Mao, T. Zhou, L. Wang, Corrosion resistance enhancement of CoCrFeMnNi high-entropy alloy fabricated by additive manufacturing, Corros. Sci. 177 (2020) 108954.

[49] S. Luo, C. Zhao, Y. Su, Q. Liu, Z. Wang, Selective laser melting of dual phase AlCrCuFeNi$_x$ high entropy alloys: Formability, heterogeneous microstructures and deformation mechanisms, Addit. Manuf. 31 (2020) 100925.

[50] J.Y. He, Q. Wang, H.S. Zhang, L.H. Dai, T. Mukai, Y. Wu, X.J. Liu, H. Wang, T. G. Nieh, Z.P. Lu, Dynamic deformation behavior of a face-centered cubic FeCoNiCrMn HEA, Science Bulletin 63(6) (2018) 362–368.

[51] P. Chen, C. Yang, S. Li, M.M. Attallah, M. Yan, In-situ alloyed, oxide-dispersion strengthened CoCrFeMnNi high entropy alloy fabricated via laser powder bed fusion, Mater. Des. 194 (2020) 108966.

[52] F. Haftlang, H.S. Kim, A perspective on precipitation-hardening high-entropy alloys fabricated by additive manufacturing, Mater. Des. 211 (2021) 110161.

[53] Y.K. Kim, J. Choe, K.A. Lee, Selective laser melted equiatomic CoCrFeMnNi high-entropy alloy: microstructure, anisotropic mechanical response, and multiple strengthening mechanism, J. Alloys Compd. 805 (2019) 680–691.

[54] Y.M. Wang, T. Voisin, J.T. McKeown, J. Ye, N.P. Calta, Z. Li, Z. Zeng, Y. Zhang, W. Chen, T.T. Roehling, R.T. Ott, M.K. Santala, P.J. Depond, M.J. Matthews, A.V. Hamza, T. Zhu, Additively manufactured hierarchical stainless steels with high strength and ductility, Nature Mater. 17 (2018) 63–71.

[55] F. Yang, L. Dong, L. Cai, X. Hu, F. Fang, Mechanical properties of FeMnCoCr high entropy alloy alloyed with C/Si at low temperatures, J. Alloys Compd. 859 (2021) 157876.

[56] W. Wu, R. Zhou, B. Wei, S. Ni, Y. Liu, M. Song, Nanosized precipitates and dislocation networks reinforced C-containing CoCrFeNi high-entropy alloy fabricated by selective laser melting, Mater. Charact. 144 (2018) 605–610.

Journal Pre-proof

[57] J.M. Park, E.S. Kim, H. Kwon, P. Sathiyamoorthi, K.T. Kim, J.-H. Yu, H. S. Kim, Effect of heat treatment on microstructural heterogeneity and mechanical properties of 1%C-CoCrFeMnNi alloy fabricated by selective laser melting, Addit. Manuf. 47 (2021) 102283.

[58] Y. Zhu, X. Wu, Perspective on hetero-deformation induced (HDI) hardening and back stress, Mater. Res. Lett. 7 (2019) 393–398.

[59] Y. Zhu, K. Ameyama, P.M. Anderson, I.J. Beyerlein, H. Gao, H.S. Kim, E. Lavernia, S. Mathaudhu, H. Mughrabi, R.O. Ritchie, N. Tsuji, X. Zhang, X. Wu, Heterostructured materials: superior properties from hetero-zone interaction, Mater. Res. Lett. 9 (2021) 1–31.

[60] Z. Li, D. Raabe, Strong and Ductile Non-equiatomic high-entropy alloys: Design, processing, microstructure, and mechanical properties, JOM 69 (2017) 2099–2106.

[61] W. Zhang, D. Yan, W. Lu, Z. Li, Carbon and nitrogen co-doping enhances phase stability and mechanical properties of a metastable high-entropy alloy, J. Alloys Compd. 831 (2020) 154799.

[62] J.M. Park, J. Choe, H.K. Park, S. Son, J. Jung, T.S. Kim, J.H. Yu, J.G. Kim, H.S. Kim, Synergetic strengthening of additively manufactured (CoCrFeMnNi)$_{99}$C$_1$ high-entropy alloy by heterogeneous anisotropic microstructure, Addit. Manuf. 35 (2020) 101333.

[63] G.M. Karthik, E.S. Kim, P. Sathiyamoorthi, A. Zargaran, S. G. Jeong, R. Xiong, S.H. Kang, J.-W. Cho, H.S. Kim, Delayed deformation-induced martensite transformation and enhanced cryogenic tensile properties in laser additive manufactured 316L austenitic stainless steel, Addit. Manuf. 47 (2021) 102314.

[64] J.-M. Kim, H.-H. Jin, J. Kwon, S.H. Kang, B.-S. Lee, Effects of cellular segregation for high strength and ductility of additively manufactured 304L stainless steel, Mater. Charact. 194 (2022) 112364.

[65] J. Liu, C. Chen, Q. Feng, X. Fang, H. Wang, F. Liu, J. Lu, D. Raabe, Dislocation activities at the martensite phase transformation interface in metastable austenitic stainless steel: An in-situ TEM study, Mater. Sci. Eng. A 703 (2017) 236–243.

[66] I. Karaman, H. Sehitoglu, K. Gall, Y.I. Chumlyakov, H.J. Maier, Deformation of single crystal Hadfield steel by twinning and slip, Acta Mater. 48 (2000) 1345–1359.

[67] J. Wang, N. Stanford, A critical assessment of work hardening in TWIP steels through micropillar compression, Mater. Sci. Eng. A 696 (2017) 42–51.

[68] E.J. Seo, J.K. Kim, L. Cho, J. Mola, C.Y. Oh, B.C. De Cooman, Micro-plasticity of medium Mn austenitic steel: Perfect dislocation plasticity and deformation twinning, Acta Mater. 135 (2017) 112–123.

[69] Z.Y. Liang, Y.Z. Li, M.X. Huang, The respective hardening contributions of dislocations and twins to the flow stress of a twinning-induced plasticity steel, Scr. Mater. 112 (2016) 28–31.

Journal Pre-proof

CRediT authorship contribution statement

Ali Chabok: Conceptualization, Methodology, Investigation, Data curation, Formal analysis, Visualization, Validation, Writing – original draft. **Wei Zhang**: Conceptualization, Methodology, Investigation, Data curation, Formal analysis, Visualization, Validation, Writing – original draft. **Jiajia Shen**: Data curation, Investigation, Formal analysis, Writing – review & editing. **João P. Oliveira**: Investigation, Writing – review & editing. **Hui Wang**: Data curation, Formal analysis. **Shaochuan Feng**: Investigation, Methodology, Writing – review & editing. **Norbert Schell**: Resources. **Bart J. Kooi**: Supervision, Formal analysis, Writing – review & editing. **Yutao Pei**: Funding acquisition, Conceptualization, Methodology, Supervision, Formal analysis, Writing – review & editing.

Declaration of competing interest

The authors declare that they have no known competing financial interests or personal relationships that could have appeared to influence the work reported in this paper.

Journal Pre-proof